

Reaction Dynamics of Zr and Nb with Ethylene

Peter A. Willis, Hans U. Stauffer, Ryan Z. Hinrichs, and H. Floyd Davis*

Department of Chemistry and Chemical Biology, Baker Laboratory, Cornell University, Ithaca, New York 14853-1301

Received: December 8, 1998; In Final Form: March 11, 1999

The reactions of transition metal (M) atoms Zr and Nb with ethylene (C_2H_4) were studied using the technique of crossed molecular beams. Angular and velocity distributions of MC_2H_2 products following H_2 elimination were measured at collision energies between 5 and 23 kcal/mol using electron impact and 157 nm photoionization mass spectrometry. Photodepletion studies identify that the atomic reactants are predominantly in their ground electronic states and that the observed MC_2H_2 products result primarily from reactions of these ground-state atoms. Center-of-mass product angular distributions derived from the data indicate that reactions involve the formation of intermediate complexes having lifetimes longer than their rotational periods. Product translational energy distributions demonstrate that a large fraction of excess available energy is channeled into product internal excitation. Wide-angle nonreactive scattering of metal atom reactants following decay of long-lived MC_2H_4 association complexes was also observed for both transition metal reactants at collision energies ≥ 9 kcal/mol, with approximately 36% of the initial translational energy converted into C_2H_4 internal excitation. At collision energies of ≤ 6 kcal/mol, nonreactive scattering of Zr from ZrC_2H_4 decay was found to be negligible, whereas this channel was clearly observed for Nb. RRKM modeling of the competition between decay of MC_2H_4 complexes back to $M + C_2H_4$ and C–H insertion forming HMC_2H_3 indicates that there exists an adiabatic potential energy barrier for $M + C_2H_4$ association in the case of Zr and that the transition state for this process is tighter than for the analogous process in $Nb + C_2H_4$. The barrier for $Zr + C_2H_4$ association is attributed to the repulsive s^2 ground state configuration of Zr, whereas for Nb the s^1 ground state configuration results in no barrier for association. The absence of decay of ZrC_2H_4 back to $Zr + C_2H_4$ at low collision energies indicates that the barrier for C–H insertion forming $HZrC_2H_3$ lies below the barrier for $Zr + C_2H_4$ association. This opens up the possibility that direct C–H insertion without initial ZrC_2H_4 formation may play an important role.

I. Introduction

The interaction of transition metal centers with alkenes plays an important role in a variety of homogeneous and heterogeneous catalytic processes, such as hydrogenation of unsaturated hydrocarbons and polymerization of olefins.^{1–3} For example, Ziegler–Natta catalysis is used to produce more polyethylene annually than any other organic chemical.¹ However, at present, the mechanisms governing these processes are still not well understood. One approach toward a greater understanding of these systems is to study model chemical reactions lacking the complicating effects of ligands and solvent.^{4,5} Ab initio and density functional calculations facilitate systematic studies of reactivities across entire rows of bare transition metal atoms,⁴ as well as the effects of covalent ligands on these reactivities.⁵ By studying trends in barrier heights and reaction energetics in such model systems, theory has begun to provide fundamental insight into how electronic configuration and orbital occupancy control transition metal–hydrocarbon reactivity.^{4–7}

Extensive studies have been performed on reactions involving transition metal *cations* with small hydrocarbons and other molecules,^{8–10} particularly by Armentrout and co-workers, using guided ion beam tandem mass spectrometry.^{9,10} The mass-selected transition metal cations are accelerated into a collision cell containing a neutral target gas, and the reaction cross-

sections for competing channels are determined as a function of collision energy. An analysis of resulting data yields a wealth of mechanistic information, as well as barrier heights for reaction and bond dissociation energies.

Because of long-range ion-induced dipole forces, potential energy surfaces (PES) for transition metal *ion* reactions are highly attractive.^{8,11} In the case of neutral transition metal atoms, interactions occur at a much shorter range and potential energy barriers are comparable to the available energy. The reaction dynamics and product branching ratios are expected to be very sensitive to the topography of the PES.¹¹ Therefore, the interactions of neutral transition metal atoms with hydrocarbon molecules are expected to more closely resemble those in transition metal complexes important in homogeneous catalysis.¹¹

Neutral transition metal atom reactions with small hydrocarbons have been studied in the gas phase using both flow tube techniques^{11–14} and laser photolysis–laser fluorescence methods.^{15–17} In the flow tube experiments, the metal (M) + hydrocarbon reactivity was measured at 300 K in 0.5–1.1 Torr of He.^{11–14} Metal atoms were created by sputtering from a solid metal sample or by laser ablation and were thermalized by collisions with He carrier gas before mixing downstream with hydrocarbon gas. By monitoring the depletion of metal atom number density using laser induced fluorescence (LIF) as a function of

* To whom correspondence should be addressed: e-mail, hfd1@cornell.edu.

hydrocarbon pressure, pseudo-first-order rate constants for $M + \text{hydrocarbon}$ reactions have been determined.^{11–13} These rate constants include contributions from bimolecular elimination reactions as well as termolecular processes. In nearly all experiments carried out to date, the chemical reaction products were not detected, but were inferred by comparison to theoretical models. Studies of this sort have shown that under low-pressure conditions in which termolecular processes do not play a major role, a number of second row transition metal atoms undergo C–H insertion reactions with ethylene and other hydrocarbons, ultimately leading to H_2 elimination.^{11–14} Recently, the ZrC_2H_2 product from the $\text{Zr} + \text{C}_2\text{H}_4$ reaction was detected directly using 157 nm photoionization by Wen and co-workers.¹⁴ These experimental studies have facilitated direct comparison with theoretical predictions.^{4,5,12,13,18,19}

In the laser photolysis–laser fluorescence technique, metal atoms are produced via multiphoton dissociation (MPD) of an appropriate volatile metal complex precursor such as $\text{Fe}(\text{CO})_5$.^{15–17} A tunable laser probes the population of metal atoms by LIF as a function of delay time after the MPD laser. Using this technique, the binding energy of the π -bonded NiC_2H_4 complex, a theoretical benchmark,^{20–22} was found to be 35.5 ± 5 kcal/mol.^{15b} Although thermodynamic quantities are now fairly well-known for many $M\text{--H}$ and $M\text{--CH}_3$ systems,⁹ relatively few other bare transition metal–ligand binding energies have been determined experimentally.

We have recently begun an experimental program to study the reactivity of neutral transition metal atoms with hydrocarbons under single-collision conditions using the technique of crossed molecular beams.^{23–25} Mass spectrometry facilitates the unambiguous detection of the neutral chemical products from bimolecular reactions at well-defined collision energies. Using the seeding technique, we are able to study these neutral reactions over a relatively wide range of collision energies. Thus, even reactions with substantial endoergicity or potential energy barriers may be studied for direct comparison to theoretical predictions. Measurements of product velocity and angular distributions are also carried out, providing insight into the reaction mechanism. This experimental technique also facilitates studies of nonreactive scattering events, which provide important complementary insight into the nature of the bimolecular process that cannot be obtained using other methods. Here we describe a study of the interactions of two early second-row ground-state transition metal atoms (Zr and Nb) with the simplest unsaturated hydrocarbon, ethylene (C_2H_4).

A. Formation of $M\text{--C}_2\text{H}_4$ Complexes. Previous experimental studies have established that the second-row transition metal atoms are more reactive than the first row.^{11–13} Because most first-row transition metal atoms have filled 4s orbitals that are larger than the 3d orbitals, the ground-state $d^{n-2}s^2$ configurations of most first-row atoms somewhat resemble noble gas atoms. When these atoms approach ethylene, large potential barriers give rise to net repulsive interactions.

The interaction of second-row transition metal atoms with ethylene proves more interesting. Here, the 5s and 4d orbitals are comparable in both size and energy, leading to a variety of ground-state orbital occupancies ($d^{n-2}s^2$ for Y, Zr, Tc, and Cd, $d^{n-1}s^1$ for Nb, Mo, Ru, Rh, and Ag, and $d^n s^0$ for Pd). The simplest model for metal–ethylene bonding is the Dewar–Chatt–Duncanson (DCD) model,²⁶ involving two simultaneous bonding interactions. The first bond, a σ -bond, involves transfer of electron density from the alkene $\text{C}=\text{C}$ π -orbital to symmetry-allowed unoccupied orbitals of the metal. This is favored by s^1 or s^0 orbital occupancy on the metal atom. The second bond is

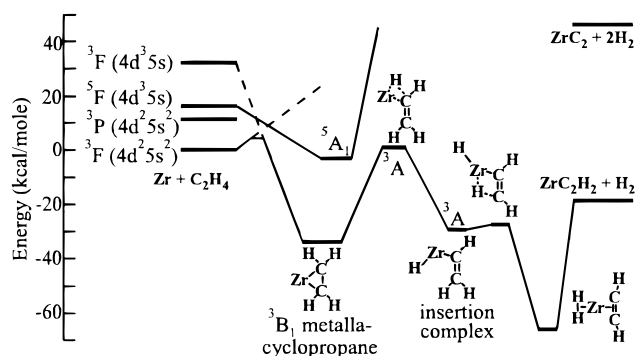


Figure 1. Reaction coordinate for Zr + ethylene system. Note that the barrier for metallacyclop propane formation is inferred from the present work. All other stationary points from ref. 13.

a π -bond, involving back-donation from a metal d orbital to the empty alkene $\text{C}=\text{C}$ π^* antibonding orbital. This bonding interaction is optimized for doubly occupied d orbitals.

Ab initio calculations indicate that sd hybridization of the transition metal center promotes bond formation in the DCD mechanism.²¹ However, only certain electron configurations on the metal allow for sd hybridization, namely, $s^1 d^{n-1}$ configurations in which the s and d electrons to be hybridized have opposite spins.^{21a} This state, which correlates diabatically to the ground state of the complex, is not in general the ground state of the metal atom, but rather a low-lying, electronically excited, low-spin state. In most cases, the ground state of the metal atom ($s^2 d^{n-2}$ or high-spin $s^1 d^{n-1}$) correlates diabatically to an excited-state MC_2H_4 complex that may be either attractive or repulsive. The avoided crossing of these two diabatic curves may lead to a small adiabatic barrier for association.¹¹

B. Zr + C_2H_4 . Ab initio calculations for various stationary points along the reaction pathway of $\text{Zr} + \text{C}_2\text{H}_4 \rightarrow \text{ZrC}_2\text{H}_2 + \text{H}_2$ yield the energetics depicted in Figure 1.¹³ For transition metal atoms on the left-hand side of the periodic table, such as Nb and Zr, the low-spin ground-state MC_2H_4 complexes have been described as “metallacyclop propane” having a C–C single bond and two covalent M–C bonds.¹⁸ In the case of Zr, calculations indicate that the triplet ground-state metallacyclop propane has a Zr– C_2H_4 distance of 2.07 Å and a C–C bond length of 1.52 Å.¹⁸ This C–C bond length is comparable to that in ethane (1.54 Å), which is considerably longer than in free ethylene (1.34 Å). The ZrC_2H_4 metallacyclop propane species lies at a substantially lower energy than the high-spin excited-state complex, which is better described as a π -complex with a shorter C–C bond (1.42 Å) and a relatively long Zr– C_2H_4 equilibrium distance (2.39 Å).¹⁸ For the purposes of this paper, when the distinction between the ground-state metallacyclop propane and excited state π -complex is not important to the discussion, any intermediate species having four intact C–H bonds will be denoted by the molecular formula MC_2H_4 . Intermediate species resulting from C–H insertion, on the other hand, will be denoted HMC_2H_3 or $\text{H}_2\text{MC}_2\text{H}_2$.

A key step in the reaction of transition metal atoms with hydrocarbons involves insertion of the metal into a C–H bond (shown for the case of Zr in Figure 1).^{13,19} In reactions of transition metal atoms with saturated hydrocarbons, such as methane (CH_4) or ethane (C_2H_6), insertion is expected to be a direct process without significant participation of the very weakly bound $M\text{--CH}_4$ or $M\text{--C}_2\text{H}_6$ σ -complexes.¹³ In reactions with unsaturated hydrocarbons such as ethylene, on the other hand, the MC_2H_4 complex represents a deep minimum on the potential energy surface. Insertion of a transition metal center into the C–H bond of a hydrocarbon molecule is favorable for

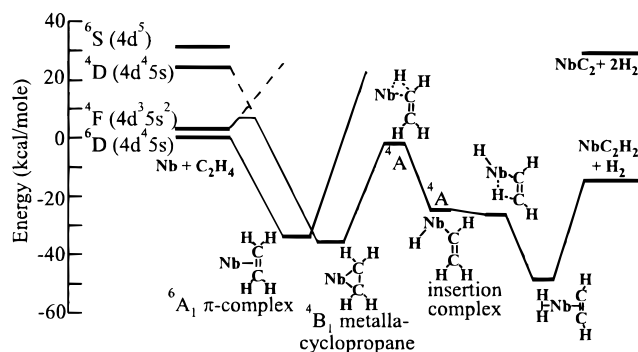


Figure 2. Reaction coordinate for Nb + ethylene system, adapted from ref 13.

low-spin electronic configurations of the metal. This is because formation of two covalent bonds in the insertion intermediate requires participation of two electrons from the metal atom (often involving *sd* hybridization) which are spin paired. This low-spin requirement is ubiquitous in insertion reactions, and explains, for instance, why O(¹D) but not O(³P) readily inserts into H₂ or CH₄.²⁷ Thus for Zr, the reaction coordinate leading to C–H insertion has triplet multiplicity, as does the metallacyclopropane complex. Consequently, C–H bond insertion may be preceded by formation of the metallacyclopropane complex. However, according to calculations,¹⁹ the optimized transition state for C–H insertion has an M–C–C bond angle greater than 120°. This transition state, calculated to lie 1.8 kcal/mol above the ground-state reactants, lies quite far from the equilibrium geometry of the MC₂H₄ complex which has an M–C–C angle considerably smaller than 90° (Figure 1).^{13,18,19} Thus the C–H bond insertion step in the Zr + C₂H₄ reaction may also occur *directly*, without first accessing the deep well associated with the M–C₂H₄ complex.

Following C–H bond insertion, a second intramolecular rearrangement may lead to formation of an H₂MC₂H₂ intermediate.¹³ This species may be either a metal–acetylene type complex (Figure 1) or a metal–vinylidene complex (H₂M=C=CH₂). To date, *ab initio* calculations have focused only on the metal–acetylene structure.¹³ Either intermediate can eliminate molecular hydrogen. Because potential energy barriers for the reverse process (insertion of transition metal centers into H₂) are generally small or nonexistent,^{4a,22} no barrier in excess of the reaction endoergicity for H₂ elimination is indicated in Figure 1. The reaction Zr + C₂H₄ → ZrC₂ + 2H₂ is endothermic by 47 kcal/mol and thus cannot occur at the collision energies used in our experiments.^{28,29}

Using a fast-flow reactor, Carroll and co-workers observed that ground-state Zr (a³F₂) reactant was depleted by ethylene at room temperature on one in every five hard-sphere collisions under low-pressure conditions where collisional stabilization of ZrC₂H₄ complexes should be negligible.^{11,13} More recently, the ZrC₂H₂ reaction product was observed via 157 nm photoionization, mass-selection, and ion detection.¹⁴

C. Nb + C₂H₄. Calculations show that for the Nb/ethylene system (Figure 2), the two most stable complexes are a low-spin ⁴B₁ ground-state metallacyclopropane (which correlates to excited quartet atomic states) and a high-spin ⁶A₁ excited state π -complex (which correlates to the ground sextet atomic states). Unlike the case for Zr, these two complexes are very similar in energy, both being bound by approximately 36 kcal/mol with respect to ground-state reactants.^{13,18} The equilibrium Nb–ethylene distances are calculated to be 2.07 Å for the ⁴B₁ ground state and 2.34 Å for the excited ⁶A₁ state.¹⁸

As in the case of Zr, the reaction coordinate leading to

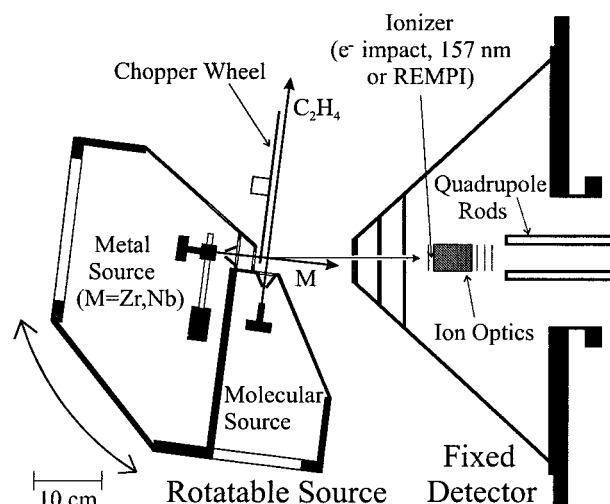


Figure 3. Cross-section of experimental apparatus in the plane of the atomic and molecular beams.

dehydrogenation products is low-spin, which in this case is of quartet multiplicity.^{13,19} However, unlike the Zr case, because the ground state of Nb is high-spin, intersystem crossing is required to access the insertion intermediate. Although diabatic curves of different spin multiplicities are more weakly coupled than those of the same multiplicity, for 4d series atoms, spin–orbit interactions can effectively couple the two states. Calculations suggest that when the system accesses the quartet reaction coordinate via a curve crossing, there are no potential energy barriers to dehydrogenation above the Nb(a⁶D) + C₂H₄ asymptote (Figure 2). Carroll and co-workers observed that at room temperature, ground-state Nb (a⁶D_{1/2}) reactant is depleted by ethylene at approximately the gas kinetic limit under low-pressure conditions where termolecular processes should be negligible.^{11,13} Thus, Nb is five times more reactive than Zr at an average collision energy of 0.9 kcal/mol.

II. Experiment

All of the experiments described in this paper were performed using a newly constructed universal crossed molecular beams apparatus (Figure 3).^{23–25} The apparatus facilitates production of two supersonic molecular beams that intersect at 90 degrees in the main vacuum chamber. The transition metal atomic beam is produced by laser ablation³⁰ from a 0.25 in. diameter rod (Alfa 99.9%) that is rotated and translated in front of a piezoelectric pulsed valve³¹ delivering an inert carrier gas. The 532 nm output (15 mJ, 7 ns, 30 Hz) from a Nd:YAG laser (Continuum Surelite 2) is focused to a 1 mm diameter spot on the surface of the metal rod. The ablated metal beam, entrained in carrier gas, passes through a skimmer and then through a second defining aperture into the main chamber. A mechanical chopper wheel (9 in. diameter, 0.5 mm slot) is spun synchronously at 210 Hz with the vaporization laser and pulsed valve for additional temporal resolution of the metal atom beam pulse. The secondary molecular beam source consists of a second piezoelectrically actuated pulsed nozzle which delivers C₂H₄ (Matheson, polymer grade, 99.9%), either neat or 20% in helium.

The entire source assembly can be rotated in a vertical plane with respect to a fixed detector (Figure 3).²⁵ This is accomplished by supporting the source assembly on two rotatable bearings with associated differentially pumped 30 in. diameter Teflon spring-loaded dynamic seals. In this configuration, a pressure (*P*) of < 2 × 10^{−6} Torr is maintained in the main chamber of the apparatus with both beams running. Because

the source is rotatable, it is necessary to continually maintain alignment of the vaporization laser on the metallic sample rod. This is accomplished by propagating the ablation laser beam along the axis of rotation of the source and then periscoping this beam into the source region using a pair of mirrors mounted on the rotating flange. In some cases, optical pumping of the resulting metal atom beam is also performed upstream of the collision region using a second rotatable periscope assembly.²³

The fixed detector unit is triply differentially pumped and equipped with electron impact ionizer, mass filter, and ion-counting electronics.^{25,32} For all experiments reported here, the mass spectrometer was operated at unit mass resolution. Because the detector is fixed in space, it is possible to introduce laser light into the ionization region of the mass spectrometer, which is held at $P \leq 2 \times 10^{-10}$ Torr during the experiment. This allows for ionization of neutral atomic species via resonance enhanced multiphoton ionization (REMPI), as well as ionization of most transition metal-containing species using 157 nm VUV excimer radiation. Product detection using photoionization methods proves especially useful, leading to greatly increased sensitivity levels over conventional electron-impact detection. A detailed account of this detection method is described elsewhere.²⁵ Briefly, the ionization laser delay is scanned relative to a time zero for reaction, defined by the chopper wheel, and total ionized products are mass-selected and counted as a function of ionization laser delay to obtain a time-of-flight (TOF) spectrum at a given angle. Both photoionization and conventional electron impact ionization methods were employed in these experiments.

The data analysis was performed using a Windows-based analysis program written at Cornell for use on a PC.³³ Velocity distributions of reactant beams were first measured by sampling the beams directly on-axis through a pinhole aperture in the front of the mass spectrometer. Using these distributions, as well as the relevant instrumental parameters for the apparatus, the beam velocities and speed ratios of the reactant beams were determined. To determine the product translational energy and angular distributions in the center-of-mass (CM) reference frame, a forward convolution technique was employed.^{33,34} This forward convolution assumes a separable CM translational energy distribution, $P(E)$, and CM angular distribution, $T(\Theta)$, in calculating the center-of-mass product flux distribution, $I_{\text{CM}}(\Theta, E) = P(E) \times T(\Theta)$. The program accepts as inputs trial distributions for $P(E)$ and $T(\Theta)$, measured beam velocities and speed ratios, known collision geometry, detector aperture sizes, etc., and then calculates *laboratory* angular distributions and TOF spectra based on calculated differential cross-sections in the laboratory frame of reference, $I_{\text{LAB}}(\theta, v)$, where v is the magnitude of the detected particle velocity in the laboratory frame. These laboratory-based quantities are determined from the calculated center-of-mass differential cross-sections $I_{\text{CM}}(\Theta, u)$ using the Jacobian relation $I_{\text{LAB}}(\theta, v) = v^2/u^2 \times I_{\text{CM}}(\Theta, u)$, where u is the magnitude of the velocity in the center-of-mass frame of reference. The calculated TOF and angular distributions are compared to the experimental ones, and the input $P(E)$ and $T(\Theta)$ are then varied until optimal agreement between the simulated and experimental data is observed.

III. Results and Analysis

A. Characterization of Zr Atomic Beam. The first stage in our investigation of the $\text{Zr} + \text{C}_2\text{H}_4$ system involved the characterization of electronic state populations present in the atomic Zr beam. Figure 4 schematically displays the experimental configuration used. The Zr beam (in He carrier gas) was crossed by the frequency-doubled output of a tunable dye laser

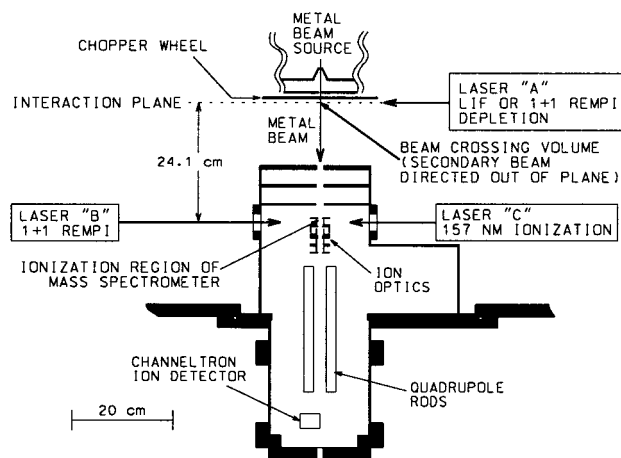


Figure 4. Cross-section of the experimental apparatus (with source at zero degree angular position) in plane of detection axis, perpendicular to molecular beam source.

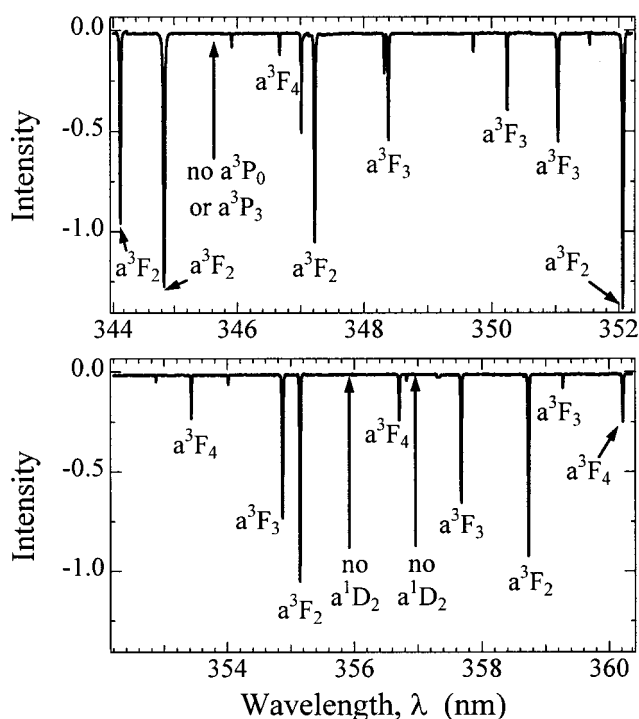


Figure 5. Fluorescence excitation spectrum of Zr beam. Peaks are labeled by the lower spin-orbit electronic state.^{35,36}

(i.e., laser "A" in Figure 4; Scanmate 2 circulating Pyridine-1 dye) at the interaction region. The fluorescence from the laser beam interaction region was imaged onto a photomultiplier tube (PMT) via a telescope, while the excitation laser wavelength was scanned. The resulting fluorescence excitation spectrum of the Zr beam is shown in Figure 5. The atomic symbols shown in Figure 5 correspond to the lower electronic state assigned to each transition. Clearly, most peaks originate from excitation out of spin-orbit levels of the ground Zr a^3F electronic state. It is notable that no peaks corresponding to well-known atomic transitions from higher metastable states, such as the a^3P or a^1D states,^{35,36} were present. For example, the 345.69 nm ($x^3S_1^0 \leftarrow a^3P_2$), 356.99 nm ($x^3S_1^0 \leftarrow a^1D_2$), and 348.40 nm ($w^1F_4 \leftarrow a^1G_4$) transitions, with $gf = 0.33$, 0.39 , and 0.89 , respectively, where f is the transition oscillator strength and g is the measured degeneracy of the excited state,³⁶ were not observed. Yet, the weaker 359.27 nm ($x^3G_3^0 \leftarrow a^3F_3$) transition ($gf = 0.034$) was clearly observed.

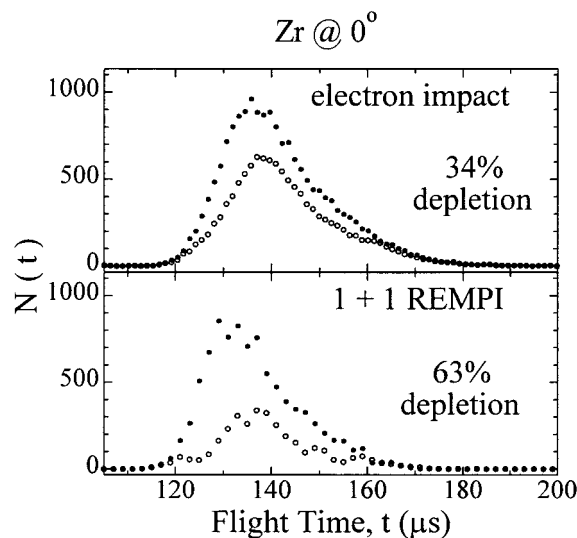


Figure 6. Zr TOF spectra at 0° recorded using electron impact ionization and 1+1 REMPI (laser “B” in Figure 4). Closed circles denote TOF when 1+1 REMPI depletion laser (laser “A” in Figure 4) is off; open circles correspond to spectra when depletion laser is on. Temporal shift between electron impact and REMPI TOF is due to slightly different flight distances in each case.

To provide quantitative insight into the composition of the Zr atomic beam, a number of photodepletion studies were carried out. The experimental arrangement is also shown in Figure 4. In these experiments, 1+1 REMPI was used to ionize a selected spin–orbit level of Zr slightly upstream of the interaction region (laser “A”). For ionization of the ground atomic 3F_1 spin–orbit states, the following wavelengths were used: 352.06 nm ($x^3G_3^0 \leftarrow a^3F_2$), 354.87 nm ($x^3G_4^0 \leftarrow a^3F_3$), and 360.22 nm ($x^3G_5^0 \leftarrow a^3F_4$).^{35,36} Ionization leads to depletion of the measured neutral beam intensity because positive ions are unable to enter the detector because of a large positive bias (+100 V) applied to the front ion lens. The fractional depletion of a given spin–orbit level due to ionization by laser “A” was determined by measuring the depletion of Zr beam intensity at the detector, again by 1+1 REMPI using a second laser in the ionization region of the mass spectrometer (laser “B” of Figure 4). By comparing the fractional depletion of a given spin–orbit state (measured by 1+1 REMPI at the detector) to the fractional depletion of the entire beam (measured by electron impact ionization at the detector), we are able to determine the absolute beam composition. For example, using relatively high laser “A” pulse energies (4 mJ), we were able to photodeplete a large fraction (63%) of the ground spin–orbit state, 3F_2 , present in the beam (Figure 6). While maintaining the same photodepletion laser intensity, we also measured the total Zr beam photodepletion using electron impact mass spectrometry, and obtained a depletion of 34%. Because depletion of 63% of the ground spin–orbit level led to 34% depletion of the total beam intensity, we conclude that 53% of the beam is in the ground spin–orbit (a^3F_2) level of the ground electronic state. Depletion TOFs for this state utilizing both electron impact ionization and 1+1 REMPI (via laser “B”) are shown in Figure 6. Using this photodepletion technique for the other spin–orbit states of the ground electronic state, the Zr beam was found to be comprised of $53(\pm 10)\%$ 3F_2 , $27(\pm 2)\%$ 3F_3 , and $5(\pm 4)\%$ 3F_4 . (Uncertainties quoted refer to a 1σ deviation in a set of 3 replicate measurements.) These measurements account for $85(\pm 11)\%$ of the total Zr population. The results of these studies did not change significantly when different carrier gases were used.

TABLE 1. Experimental Conditions for Zr + C₂H₄ Studies

Zr beam carrier gas mixture composition	C ₂ H ₄ gas mixture composition	mean collision energy (kcal/mol)
pure Ne	pure C ₂ H ₄	5.9
70% Ne/30% He	20% C ₂ H ₄ /80% He	9.1
13% Ne/87% He	20% C ₂ H ₄ /80% He	14.0
50% H ₂ /50% He	20% C ₂ H ₄ /80% He	23.1

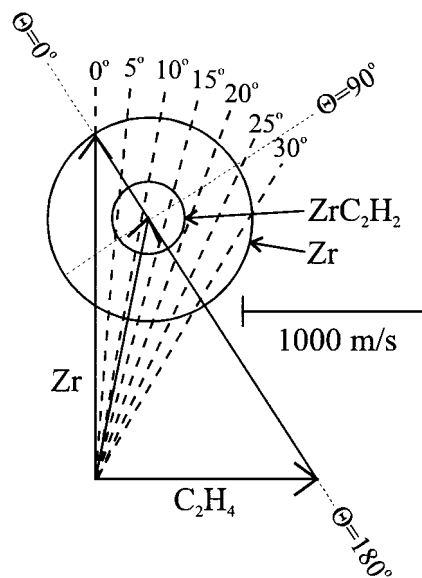


Figure 7. Newton diagram in velocity space for Zr + ethylene at 14.0 kcal/mol. Lab angle $\theta = 0^\circ$ defined as axis of Zr beam. Velocity of the center of mass of the system (at $\theta_{cm} = 11^\circ$) is indicated by a vector. Angles in the center-of-mass frame of reference, $\Theta = 0^\circ, 90^\circ$, and 180° , are also indicated.

B. Zr + C₂H₄ Reaction at 14.0 kcal/mol. We have studied the Zr + C₂H₄ reaction at several collision energies, as summarized in Table 1. For each collision energy, data sets were recorded utilizing electron impact ionization as well as VUV photoionization for product detection. Naturally occurring Zr exists as 51.5% ^{90}Zr , 11.2% ^{91}Zr , 17.2% ^{92}Zr , 17.4% ^{94}Zr , and 2.8% ^{96}Zr .³⁷ For all experiments, the lightest and most abundant Zr isotope was monitored at $m/e = 90$. Our observation of $^{90}\text{ZrC}_2\text{H}_2$ ($m/e = 116$) is in agreement with the recent observations of this channel by Wen and co-workers at an average collision energy of 0.9 kcal/mol.¹⁴

The results from an intermediate collision energy (E_{coll}), of 14.0 kcal/mol will first be presented in detail, the lower and higher collision energy data being discussed later. The measured peak beam velocities (v_{pk}) and full width at half-maximum (fwhm) values were, respectively, 1876 and 263 m/s for the Zr beam, and 1208 and 138 m/s for the C₂H₄ beam. These measured peak beam velocities and the calculated exothermicity¹³ of the reactive channel $\text{Zr} + \text{C}_2\text{H}_4 \rightarrow \text{ZrC}_2\text{H}_2 + \text{H}_2$ ($\Delta E = -18.5$ kcal/mol) yield the Newton diagram³⁸ in velocity space shown in Figure 7. The Newton diagram facilitates the transformation between the laboratory and center-of-mass frames of reference.³⁸ The two circles in the figure denote the maximum velocities of ZrC₂H₂ and Zr in the CM frame based on energy and momentum conservation. As indicated by the circles, the ZrC₂H₂ products are constrained to appear at laboratory angles (θ) ranging from 4° to 19° , where $\theta = 0^\circ$ is defined as the axis of the Zr beam. The nonreactively scattered Zr atoms, on the other hand, may appear over a wider range of laboratory angles, ranging from $\theta = -10^\circ$ to $\theta = 34^\circ$.

Product $^{90}\text{ZrC}_2\text{H}_2$ TOF spectra recorded at $m/e = 116$ using electron impact ionization over the angular range of 9° to 15°

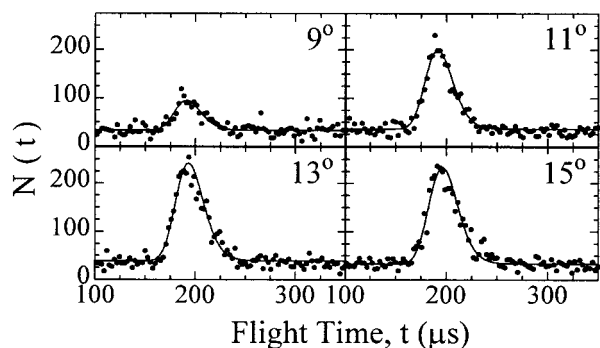


Figure 8. ZrC_2H_2 product TOF spectra ($E_{\text{coll}} = 13.7$ kcal/mol) recorded at several laboratory angles using electron impact ionization detection. Each TOF corresponds to 24 000 laser shots.

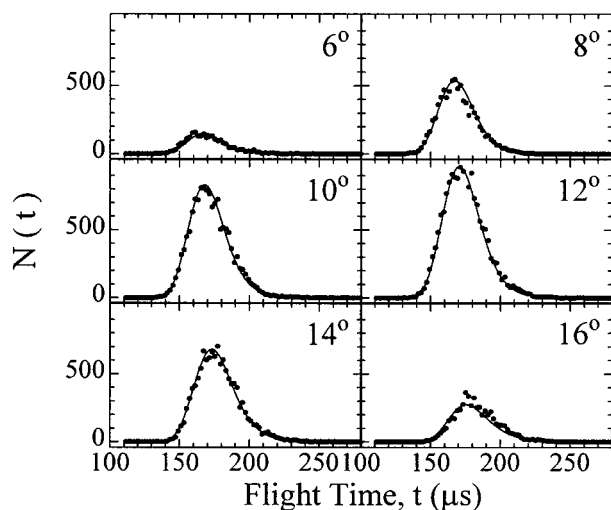


Figure 9. ZrC_2H_2 product TOF spectra ($E_{\text{coll}} = 14.0$ kcal/mol) recorded at several laboratory angles using 157 nm photoionization detection.

are shown in Figure 8. Each TOF shown represents 24 000 laser shots, corresponding to 13.3 min data acquisition time. Product TOF spectra recorded using 157 nm photoionization are shown in Figure 9. Note that the arrival times are slightly earlier than in Figure 8. This is due to the somewhat shorter flight distance to the photoionization region as well as slightly greater beam velocities used to record the data shown in Figure 9. The photoionization TOFs have a much better signal-to-noise ratio with essentially zero background, although each TOF was acquired in only 2550 laser shots (85 s of real time). The laboratory angular distribution of ZrC_2H_2 products, obtained by integrating the TOFs recorded via photoionization in one-degree laboratory angle increments, is shown in Figure 10.

The solid lines shown in Figures 8–10 are the simulated TOFs (Figures 8 and 9) and laboratory angular distribution (Figure 10) resulting from the input $P(E)$ and $T(\Theta)$ shown in Figure 11. The best match of the simulation to the data indicates a $P(E)$ that peaks slightly away from zero, extending out to the calculated maximum available energy of approximately 30 kcal/mol. The calculated laboratory angular distributions are more sensitive to the form of the $P(E)$ than the simulations of individual TOF spectra.

The dashed lines in the $P(E)$ of Figure 11 indicate the range of distributions that give satisfactory simulation of the data. The corresponding laboratory angular distributions are indicated as dashed lines in Figure 10. The laboratory angular distribution (Figure 10) drops off sharply and in a symmetric fashion away from the center of mass of the system ($\theta_{\text{cm}} \sim 11^\circ$) which is consistent with a $P(E)$ that peaks close to zero. The effect upon

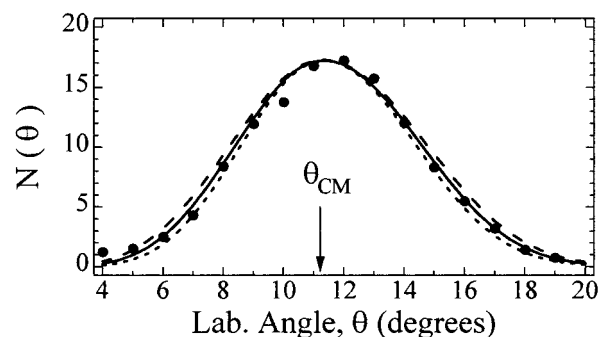


Figure 10. ZrC_2H_2 laboratory angular distribution at $E_{\text{coll}} = 14.0$ kcal/mol. Lines represent simulation of distribution using $T(\theta)$ and $P(E)$ in Figure 11. Solid line corresponds to best simulation of data. Dashed lines represent a range of acceptable fits.

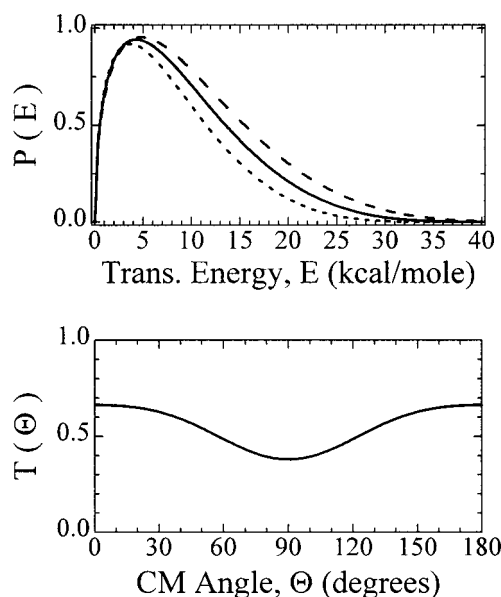


Figure 11. Center of mass distributions used for simulation of ZrC_2H_2 reactive signal at $E_{\text{coll}} = 14.0$ kcal/mol. Solid line represents “best fit” with uncertainties shown by dashed lines.

this laboratory distribution from varying how far the $P(E)$ peaks away from zero is demonstrated in Figure 12. Note that the best agreement between the experimental data and experimental fit is obtained using the $P(E)$ shown as a solid line in Figures 11 and 12. As indicated in Figure 13, the laboratory angular distribution is not properly simulated using $P(E)$ s having substantially different shapes from the optimum $P(E)$, shown again in the upper panel. Most of the available energy is therefore channeled into the internal energies of the product ZrC_2H_2 and H_2 molecules. The forward–backward symmetric nature of the CM angular distribution suggests that the reaction proceeds via one or more intermediates having lifetimes exceeding their rotational periods.^{34,38}

C. Identity of the Reactive Zr State. To identify the reactive state(s) of Zr, a series of photodepletion studies were carried out. In these experiments, the ZrC_2H_2 products were monitored at the CM angle while the Zr reactant beam was state-selectively photodepleted by 1+1 REMPI, slightly upstream (8 mm) of the reaction volume (laser “A” in Figure 4). If the photodepleted state is reactive, a decrease in ZrC_2H_2 product intensity should be observed. The fractional depletion of the product intensity provides information about the relative contribution of a given state to the total reactive signal. In some experiments, a strong electric field was used to extract the resulting ions before they crossed the molecular beam. No difference was seen in the

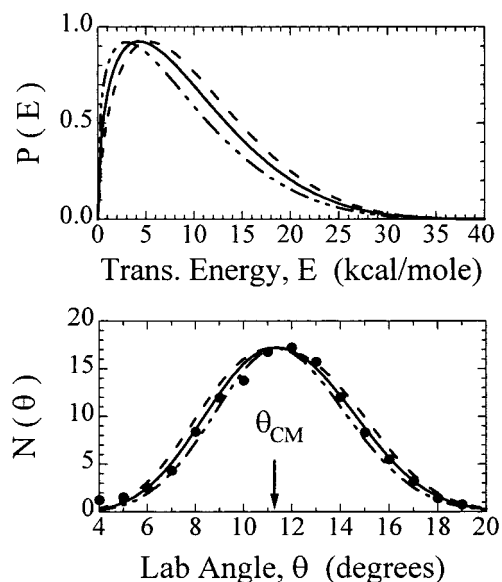


Figure 12. The upper panel shows the “best fit” $P(E)$ and two alternate $P(E)$ s having peaks at higher and lower energies. Laboratory angular distributions resulting from these $P(E)$ s are shown in bottom panel.

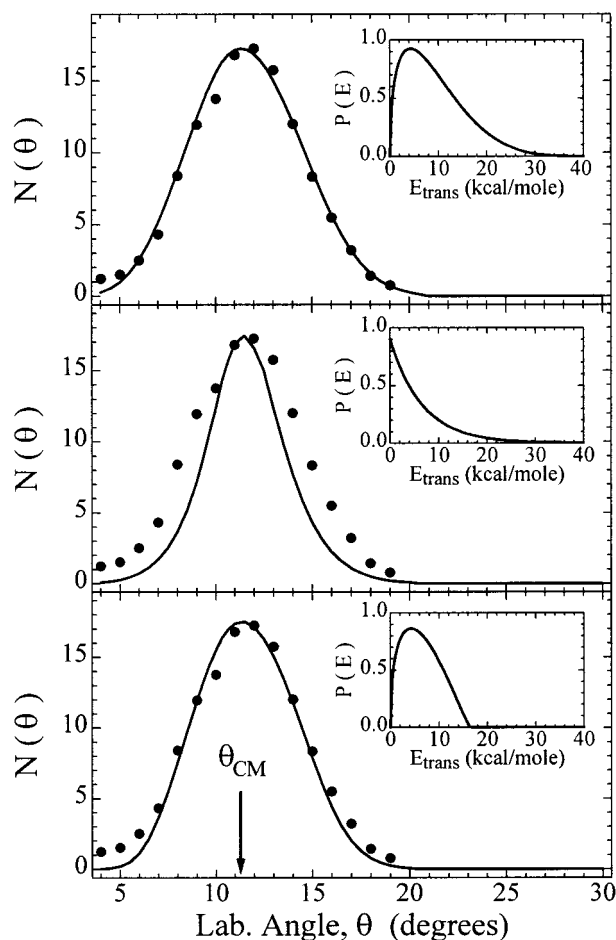


Figure 13. Simulation of ZrC_2H_2 laboratory angular distribution. Top panel shows simulation using optimum $P(E)$. Lower panels show simulations using different $P(E)$ distributions which lead to poorer simulation of angular distribution.

observed TOF data when this field was applied. This was expected because metal cations or positively charged reaction products are unable to enter the mass spectrometer because of a large applied positive DC field at the entrance to the mass spectrometer ion lenses. Owing to the much greater sensitivity

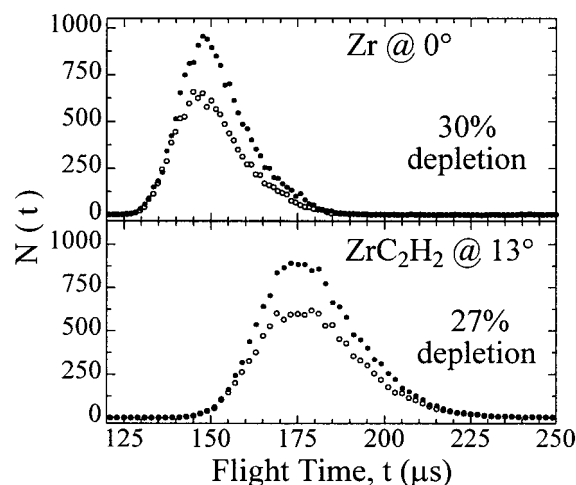


Figure 14. Photodepletion spectra of reactant Zr beam (top panel) and resulting ZrC_2H_2 signal at $\theta = 13^\circ$ (bottom panel). Open circles correspond to 1+1 REMPI depletion laser on (laser “A” in Figure 6); closed circles are for depletion laser off.

of VUV photoionization, the results presented here were carried out using this method (i.e., using laser “C” in Figure 4). However, photodepletion of reactive signal was also detected using electron impact ionization.

The depletion of reactive signal ($m/e = 116$) resulting from crossed beams experiments in which one of the ground spin-orbit states was depleted was found to be comparable in magnitude to the total depletion of the corresponding reactant Zr beam (measured by electron impact ionization). TOF spectra displaying depletion of reactive signal resulting from the $^3\text{F}_2$ ground spin-orbit state are given in the bottom panel of Figure 14. This verifies that the observed reactive signal results predominantly from reactions of *ground state* Zr atoms.

D. Nonreactive Zr + C_2H_4 Scattering at 14.0 kcal/mol.

The nonreactive channel, $\text{Zr} + \text{C}_2\text{H}_4 \rightarrow \text{Zr} + \text{C}_2\text{H}_4$, in which Zr reactants are reformed after collision and possible association with ethylene, was also examined. Collisions that result in the formation of ZrC_2H_4 complexes having lifetimes longer than a rotational period before subsequent reformation of reactants are expected to produce Zr signal at large laboratory angles, corresponding to CM angles, Θ , near 180° (Figure 7).³⁴ Zr atom ($m/e = 90$) TOF spectra at laboratory angles of 15° , 20° , and 25° (recorded using 157 nm photoionization) are shown in Figure 15. The large, slow peak in the TOF at $\theta = 15^\circ$, occurring at $t = 175 \mu\text{s}$, is due primarily to fragmentation of product ZrC_2H_2 in the mass spectrometer. This contribution to the TOF is simulated using the reactive $P(E)$ and $T(\Theta)$ discussed above (Figure 11). Fragmentation of ZrC_2H_2 to form Zr is also observed at $\theta = 20^\circ$, although only very weakly, because at this angle, the extreme edge of the reactive Newton circle (Figure 7) is being sampled. The solid lines in Figure 15 are thus comprised of two components (shown as dashed lines): fragmentation of the reactive channel and the nonreactive channel, which was best simulated using the $P(E)$ and $T(\Theta)$ shown in Figure 16. The dashed lines in Figure 16 represent the range of $P(E)$ s that are deemed to adequately model the nonreactive signal.

As expected from the Newton diagram (Figure 7), the Zr TOF recorded at $\theta = 25^\circ$ has no contribution from fragmentation of ZrC_2H_4 reaction products. Two distinct peaks are observed, which correspond to the fast and slow edges of the nonreactive Zr Newton circle. The slower peak, which corresponds to very large CM angles, Θ , is more intense than the faster peak. This

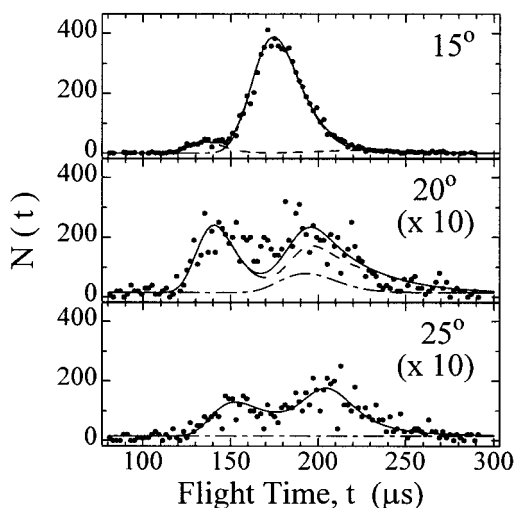


Figure 15. Nonreactively scattered Zr atom TOF spectra ($E_{\text{coll}} = 14.0$ kcal/mol).

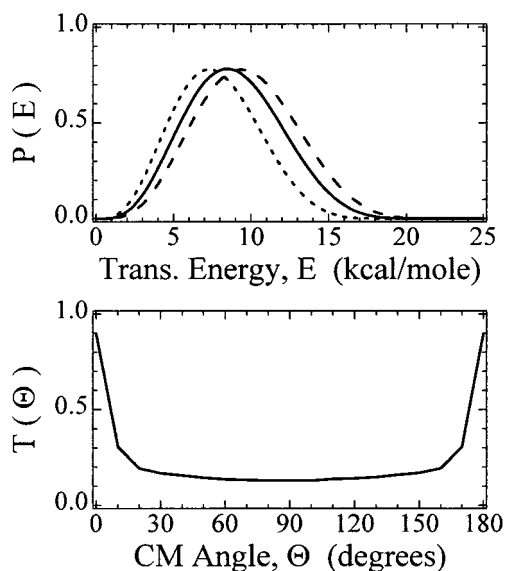


Figure 16. CM distributions for simulation of nonreactive signal ($E_{\text{coll}} = 14.0$ kcal/mol). Dashed lines in $P(E)$ represent uncertainty in simulation.

indicates that $T(\Theta)$ is sharply peaked at $\Theta = 180^\circ$, i.e., backward scattered in the CM frame relative to the incoming Zr atom (Figure 7). The $T(\Theta)$ which was found to best simulate the nonreactive Zr scattering (Figure 16) exhibits this feature. Such sharply peaked wide angle nonreactive scattering indicates the formation of a long-lived collision complex that subsequently falls apart to reform reactants.^{34,38} Although near-zero impact parameter collisions ($b \approx 0$) can also produce signal at $\Theta = 180^\circ$, such events are relatively improbable ($\pi b^2 \rightarrow 0$ as $b \rightarrow 0$) and would not lead to a sharp peak at $\Theta = 180^\circ$. A corresponding peak at $\Theta = 0^\circ$ is also expected from this nonreactive collision complex channel; however, this peak cannot be experimentally distinguished from the directly forward scattered Zr atoms that result from large impact parameter collisions. The recoil translational energy distribution, $P(E)$, has an average value, E'_{trans} , of $8.9 (\pm 1.1)$ kcal/mole. Thus, reactants are reformed with approximately 36% of the initial translational energy appearing as internal excitation of ethylene.

E. Effect of Collision Energy on Zr + C₂H₄. The Zr + C₂H₄ system was studied at three other collision energies: 5.9, 9.1, and 23.1 kcal/mol. Product ZrC₂H₂ was clearly observed at all collision energies. The $T(\Theta)$ s found to best simulate the

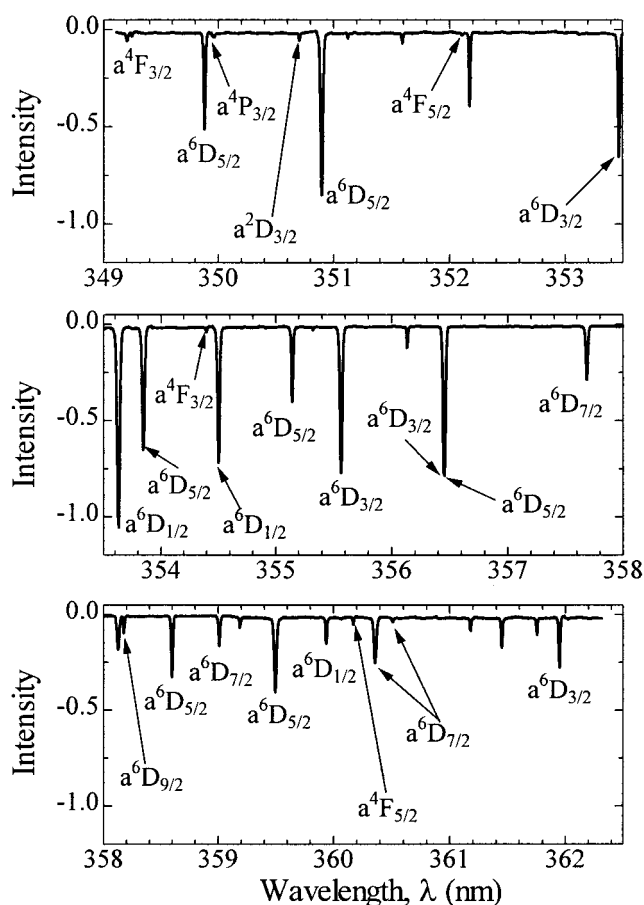


Figure 17. Fluorescence excitation spectrum of Nb atomic beam seeded in 87% He/13% Ne. Peaks are labeled by the lower spin-orbit electronic state.^{35,36}

reactive scattering data at these three collision energies were nearly identical to the best fit $T(\Theta)$ for $E_{\text{coll}} = 14.0$ kcal/mol, shown in Figure 11. The $P(E)$ s found to best simulate the data were of similar shape to the $P(E)$ found to best simulate the 14.0 kcal/mol data, although they were stretched (higher collision energy) or compressed (lower collision energy) because of the differing amounts of total energy available at the different collision energies.

For the two highest collision energies, a single $T(\Theta)$ was used for simulation of both nonreactive scattering data sets. At all collision energies, the $P(E)$ s used for best simulation of the data were the same shape, although stretched or compressed appropriately. However, as discussed in detail in section III. H., the second (slower) Zr peak corresponding to sharp backscattering at $\Theta = 180^\circ$ was *not* observed at the two lowest collision energies studied, i.e., at $E_{\text{coll}} \leq 9.1$ kcal/mol.

F. LIF Study of Nb Beam and Identity of Reactive State.

The sextet spin multiplicity of the Nb ground state makes an exhaustive population analysis of the Nb beam more difficult than for the case of Zr (which has a triplet ground state). A fluorescence excitation spectrum (Figure 17) of the Nb beam (He carrier gas seeded with 13% Ne) was acquired in the same way as described for the Zr spectrum (Figure 5), although for the longest wavelengths in the spectrum, Pyridine-2 dye was used in the Scanmate 2 dye laser. Although it is possible to assign certain peaks in the spectrum to metastable electronic states, such as a^4F , a^4P , or a^2D ,^{35,36} the total population of these states was very small.

To determine the identity of the reactive state, a photodepletion study similar to that described for the Zr system was

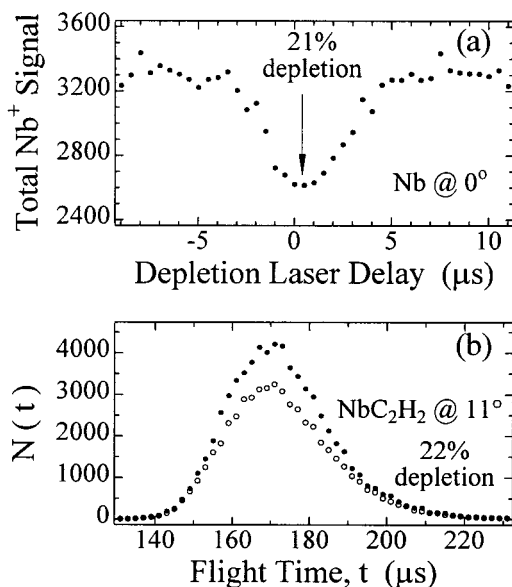


Figure 18. (a) The peak Nb atomic beam intensity at 0° as a function of 1+1 REMPI depletion laser (laser "A" in Figure 4) delay. At optimal delay, 21% of the Nb beam is depleted. (b) NbC₂H₂ reactive signal at 12° with the depletion laser on (open circles) and off (closed circles). With depletion laser set at optimal delay, 22% of the reactive signal is depleted.

TABLE 2. Experiment Conditions for Nb + C₂H₄ Studies

Nb beam carrier gas mixture composition	C ₂ H ₄ gas mixture composition	mean collision energy (kcal/mol)
pure Ar	pure C ₂ H ₄	4.8
pure Ne	pure C ₂ H ₄	6.2
70% Ne/30% He	20% C ₂ H ₄ /80% He	9.1
13% Ne/87% He	20% C ₂ H ₄ /80% He	13.5
50% H ₂ /50% He	20% C ₂ H ₄ /80% He	23.2

performed in which *two* atomic ground spin-orbit states were ionized via 1+1 REMPI using a single laser. The transitions used were 356.35 nm ($z^4D_{3/2} \leftarrow a^6D_{3/2}$) and 356.36 nm ($y^4P_{5/2}^0 \leftarrow a^6D_{5/2}$),³⁵ both of which could be accessed simultaneously by a single dye laser. These transitions were chosen because 1+1 REMPI of Nb was found to be much less efficient than for Zr, presumably because of a smaller cross-section for the ionization step. The results are illustrated in Figure 18. The upper panel illustrates the peak Nb beam intensity as a function of depletion laser delay. At the optimal depletion laser delay, it was possible to deplete a total of 21(±3)% of the total beam population by ionizing these two spin-orbit states. The lower panel indicates a 22(±3)% depletion of NbC₂H₂ product signal at $\theta = 11^\circ$ resulting from this optimal delay. This result demonstrates that the predominant reactive state is the ground a^6D state.

G. Nb + C₂H₄ at 13.5 kcal/mol. As was seen for the Zr reactions studied, dehydrogenation products (i.e., NbC₂H₂, $m/e = 119$) were observed at all collision energies (Table 2). For the intermediate collision energy of 13.5 kcal/mol, the measured peak beam velocities (v_{pk}) and fwhm values were, respectively, 1890 and 228 m/s for the Nb beam and 1208 and 138 m/s for the C₂H₄ beam. The Newton diagram for this system is very similar to that of the corresponding Zr system (Figure 7), although the exothermicity has been calculated¹³ to be slightly less (14.4 kcal/mol), giving rise to a slightly smaller NbC₂H₂ Newton circle. Recorded NbC₂H₂ product data (using 157 nm photoionization) are displayed as TOF spectra (Figure 19) and in the lab angular distribution (Figure 20).

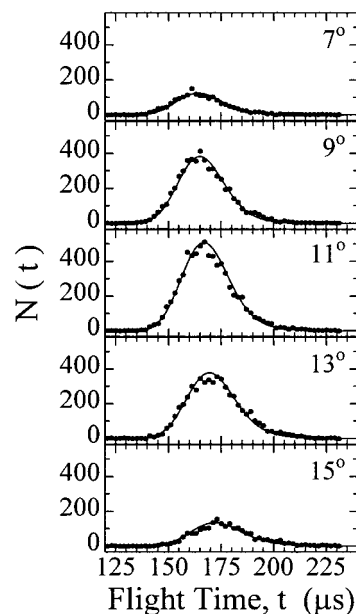


Figure 19. NbC₂H₂ product TOF spectra (13.5 kcal/mol) recorded at several laboratory angles using 157 nm photoionization detection. Solid lines are simulations using CM functions given in Figure 21.

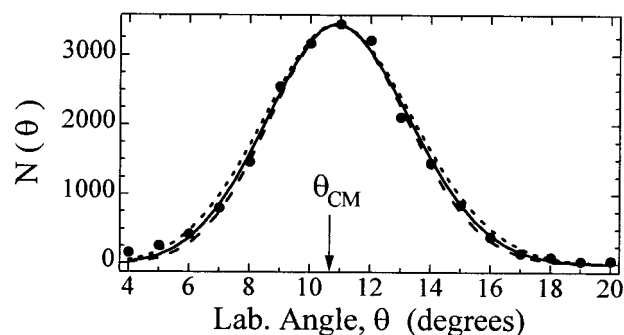


Figure 20. NbC₂H₂ laboratory angular distribution (13.5 kcal/mol data set). Solid line represents "best fit" simulation using solid line $P(E)$ shown in Figure 21. Dashed lines correspond to alternate $P(E)$ distributions also shown in Figure 21.

The solid lines shown in Figures 19 and 20 are the simulated TOFs and laboratory angular distribution resulting from the input $P(E)$ and $T(\Theta)$ of Figure 21. The dashed lines shown in the figure represent the range of acceptable $P(E)$ s that simulate the observed data, giving rise to the dashed angular distributions of Figure 20. The similarity between these input functions and those used to simulate the Zr reactive signal suggests that, again, most of the available energy is channeled into internal energy of the NbC₂H₂ + H₂ products which are formed from decay of one or more long-lived intermediates.

Nonreactively scattered Nb atom TOFs for the intermediate collision energy of 13.5 kcal/mol (detected via 157 nm photoionization) at laboratory angles of 15°, 20°, 25°, and 30° are shown in Figure 22. The $P(E)$ and $T(\Theta)$ used to simulate the data (Figure 23) are qualitatively quite similar to those found for Zr at $E_{coll} = 14.0$ kcal/mol. The $T(\Theta)$ indicates that a substantial fraction of Nb atoms are strongly backward scattered in the CM frame relative to the incoming Nb reactant.

H. Effect of Translational Energy on Nb and Zr Collisions with C₂H₄. As displayed in Table 2, the Nb + C₂H₄ reaction was also studied at a range of collision energies. As was the case in the Zr system, reactive dehydrogenation products are clearly observed at all collision energies. For all data sets, the $T(\Theta)$ resulting in the best simulation of reactive signal does

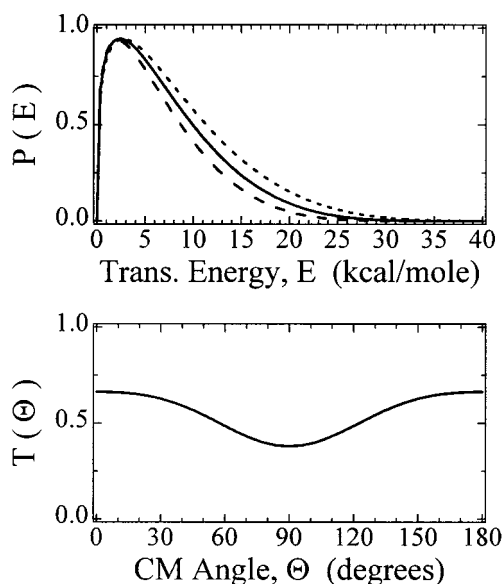


Figure 21. CM distributions used for simulation of NbC_2H_2 reactive signal from 13.5 kcal/mol data set. Solid line $P(E)$ represents “best fit” and dashed lines indicate uncertainties.

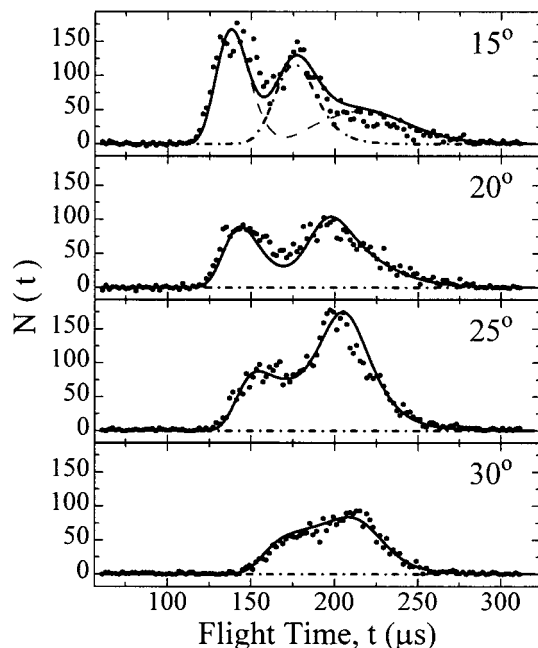


Figure 22. Nonreactively scattered Nb atom TOF spectra at 13.5 kcal/mol. Solid line represents simulation of data using the CM distributions shown in Figure 23. Contribution to 15° TOF at $t = 175 \mu\text{s}$ is due to fragmentation of NbC_2H_2 upon 157 nm photoionization.

not change as a function of collision energy. The $T(\Theta)$ s for best simulation of nonreactively scattered Nb atoms are also found to be quite similar for all data sets, sharply peaking at $\Theta = 180^\circ$ at all collision energies studied. The resulting $P(E)$ s for best simulations of data (reactive and nonreactive) are found to be stretched or compressed proportionately with increasing or decreasing collision energy supplied.

Figure 24 shows the effect of collision energy on the wide-angle scattering of Zr and Nb atoms off of C_2H_4 . At all three collision energies shown, TOFs were recorded at laboratory angles ($\theta = 25^\circ$ or 30°) where significant backward scattering in the CM frame ($\Theta = 180^\circ$) relative to the incoming metal atom from decay of long-lived complexes should be evidenced by an intense slower peak in the TOF spectra. To improve the

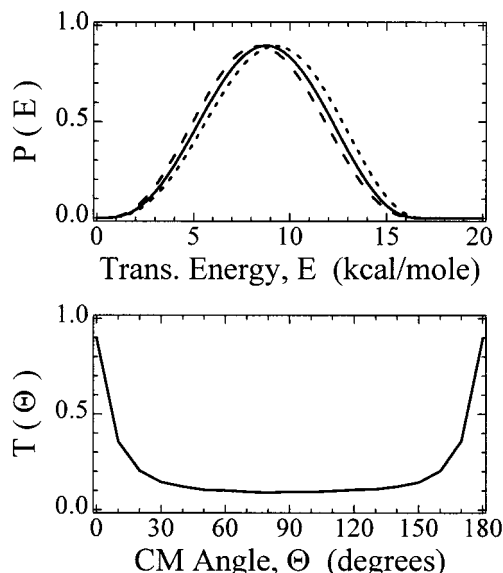


Figure 23. $P(E)$ and $T(\Theta)$ for simulation of Nb nonreactive signal (13.5 kcal/mol). Dashed lines in $P(E)$ represent uncertainty in simulation.

signal-to-noise ratio and to remove any contribution from fragmentation of ZrC_2H_2 products, the wide-angle Zr TOF spectra were also taken using 1+1 REMPI ($\lambda = 352.06 \text{ nm}$) to detect the ground-state Zr $a^3\text{F}_2$ atoms at the detector. The Newton diagram shown in velocity space schematically represents the nonreactive scattering of Zr and Nb at $E_{\text{coll}} \approx 14 \text{ kcal/mol}$. Note that the fast peak corresponds to $\Theta \approx 100^\circ$, while the slow peak corresponds to $\Theta \approx 180^\circ$. Experimental Nb and Zr TOF spectra at $E_{\text{coll}} \approx 14 \text{ kcal/mol}$, taken at $\theta = 25^\circ$, are shown in the top panel. At 14 kcal/mol, the Nb and Zr TOF spectra are similar, with two peaks clearly evident. The lower panels show Zr and Nb TOF spectra taken at analogous angles for $E_{\text{coll}} \approx 9$ and 6 kcal/mol. For Nb, the two peaks are observed down to the lowest collision energy studied. However, for Zr, at $E_{\text{coll}} = 9.1 \text{ kcal/mol}$ the slower peak is very weak and at 5.8 kcal/mol it is absent. We conclude that at low collision energies, the sharp backscattering ($\Theta = 180^\circ$) of Zr atoms resulting from decay of long-lived complexes is absent.

We have also compared the absolute reactivities of the two atoms with ethylene. For each atom, the total MC_2H_2 product flux was normalized to the reactant atomic beam intensity at each collision energy studied. In this way, the ratio of the reactivity of Zr to Nb as a function of collision energy was determined. As displayed in Figure 25, the reactivity of Zr increases relative to that of Nb as the collision energy is increased.

IV. Discussion

A. Angular Momentum in Nonreactive Scattering. Conservation of angular momentum through the nonreactive inelastic collision is represented by eq 1:

$$\mathbf{L} + \mathbf{J} = \mathbf{J}^* = \mathbf{L}' + \mathbf{J}' \quad (1)$$

where \mathbf{J} and \mathbf{J}' represent the rotational angular momenta of the initial reactant and reformed reactant molecules, respectively. \mathbf{L} and \mathbf{L}' are the relative orbital angular momenta of the colliding and recoiling bodies, and \mathbf{J}^* is the angular momentum of the intermediate complex. The efficient rotational cooling of the supersonic expansion will leave ethylene with very little average rotational angular momentum ($\mathbf{J} < 5\hbar$).³⁹ For a colliding pair,

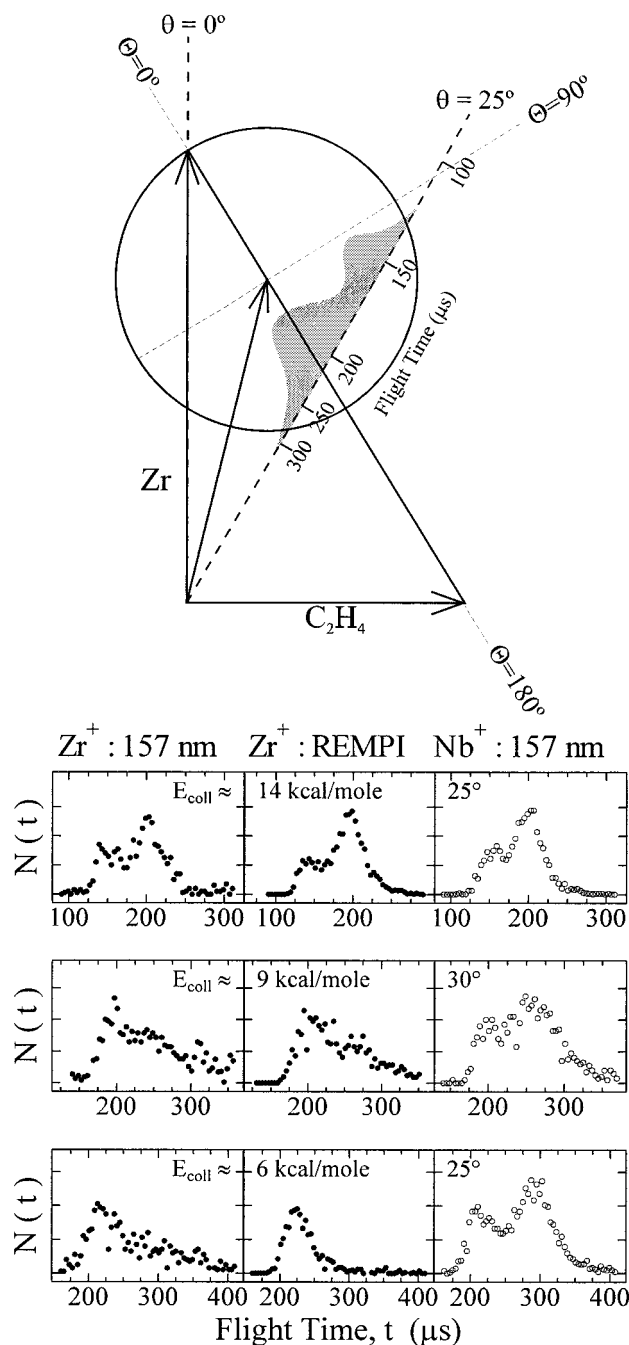


Figure 24. Top: Newton diagram for nonreactive collisions at $E_{\text{coll}} \approx 14$ kcal/mol. Bottom: TOF spectra for Zr and Nb + C₂H₄ at 14, 9, and 6 kcal/mol. Note that at 6 kcal/mol, the slower peak disappears in the Zr system.

the magnitude of the orbital angular momentum (L) is

$$L = \mu v b \quad (2)$$

where μ is the reduced mass, v is the relative velocity, and b the collision impact parameter. To estimate the maximum impact parameter that leads to complex formation, we assume a standard "capture model".⁴⁰ Let us examine one particular system in detail: Nb + C₂H₄ at 13.5 kcal/mol. The attractive long-range interaction potential between the Nb and ethylene is approximated by a C_6 potential, i.e.,

$$V(r) = -\frac{C_6}{r^6} \quad (3)$$

with $C_6 = 10.6 \times 10^3 \text{ \AA}^6 \text{ kcal/mole}$ for the Nb/ethylene system.^{41,42}

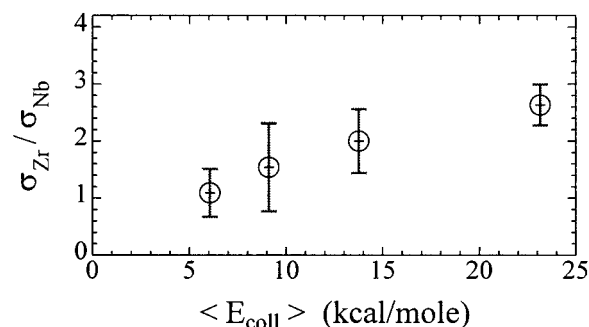


Figure 25. Ratio of absolute reactivities of Zr to Nb with ethylene as a function of collision energy. Error bars represent 1 σ deviation in a set of three replicate measurements.

The radial distance between the Nb + C₂H₄ pair is governed by motion under the influence of an effective potential given by eq 4:

$$V_{\text{eff}} = V(r) + \frac{L^2}{2\mu r^2} \quad (4)$$

Thus, at increasing impact parameters, the magnitude of the repulsive centrifugal potential ($L^2/2\mu r^2$) begins to exceed the attractive dispersive potential $V(r)$, leading to a barrier in V_{eff} . Using this model, the maximum impact parameter b_{max} capable of surmounting the resulting centrifugal barrier to association is given⁴⁰ by eq 5:

$$b_{\text{max}} = \left[\frac{3}{2^{2/3}} \right]^{1/2} \left(\frac{C_6}{E_{\text{coll}}} \right)^{1/6} = 1.375 \left(\frac{C_6}{E_{\text{coll}}} \right)^{1/6} \quad (5)$$

Hence $b_{\text{max}} = 4.2 \text{ \AA}$ for the collision energy of $E_{\text{coll}} = 13.5$ kcal/mol. Furthermore, using the measured most probable relative velocity $|\mathbf{v}| = 2243 \text{ m/s}$, eq 2 gives $|\mathbf{L}_{\text{max}}| = |\mu \mathbf{v} b_{\text{max}}| = 319\hbar$.

For long-lived complexes, the shape of the $T(\Theta)$ is determined only by the disposal of angular momentum into the reformed reactants.³⁴ For systems such as this where $\mathbf{L}_{\text{max}} \gg \mathbf{J}$, the statistical complex model³⁴ reveals that the shape of the $T(\Theta)$ is related to a single parameter, X , given by the ratio

$$X = \frac{|\mathbf{L}_{\text{max}}|}{\langle M' \rangle_{\text{rms}}} \quad (6)$$

Here, M' is defined as the projection of \mathbf{J}^* onto the relative recoil velocity vector \mathbf{v}' and $\langle M' \rangle_{\text{rms}}$ refers to the root-mean-square (rms) average value of M' . For prolate rotors (i.e., $I_x = I_y > I_z$) in which the decomposition occurs directly along the principal axis I_z ($\mathbf{v}' \parallel I_z$), the rms value of M' is zero and $X \rightarrow \infty$. Classically, this results in a $T(\Theta)$ with a $1/\sin(\Theta)$ form, extending to infinity at $\Theta = 0^\circ$ and 180° .³⁴ Decomposition with greater rms values of M' (i.e., smaller values of X), results in a less sharply peaked $T(\Theta)$. A comparison of the $T(\Theta)$ used for best simulation of our data (Figure 16) to the $T(\Theta)$ calculated from the statistical complex model³⁴ suggests that the Nb + C₂H₄ system decomposes along the principal axis of a prolate rotor complex with $X = 8(\pm 1)$. Using $|\mathbf{L}_{\text{max}}| = 319\hbar$, this yields $\langle M' \rangle_{\text{rms}} = 40(\pm 5)\hbar$. This is consistent with the calculated nearly-prolate geometry¹⁸ of the ground-state NbC₂H₄ complex, having moments of inertia $I_x = 113 \text{ amu} \cdot \text{\AA}^2$, $I_y = 95.7 \text{ amu} \cdot \text{\AA}^2$, and $I_z = 24.3 \text{ amu} \cdot \text{\AA}^2$ decomposing to reactant Nb + C₂H₄ along its

principal moment of inertia I_z , i.e., along the Nb/C=C bond axis. Hence a large fraction of the total angular momentum (J^*) in the complex appears as relative orbital angular momentum of the reformed reactants, L' .

B. The Absence of Zr Nonreactive Scattering at $E \leq 9.1$ kcal/mol. As indicated in Figure 24, the difference between the Nb and Zr nonreactive scattering signal at low collision energies is quite striking. In the case of Zr at collision energies of 9.1 and 5.8 kcal/mol, the faster peak in each TOF corresponds to those scattering events leading to smaller-angle deflection ($\Theta \approx 100^\circ$) of Zr atoms in the CM frame of reference. A small broad tail is also observed at longer times, indicating that some "direct rebound" collisions of Zr off of C_2H_4 at small impact parameters can also be detected at these wider angles. The important observation is that the sharply backward-scattered component ($\Theta \approx 180^\circ$) indicative of long-lived complexes is relatively weak at 9.1 kcal/mol and is absent at 6.0 kcal/mol. This contrasts the observed nonreactive scattering of Nb, which exhibits sharply backward scattered signal at all collision energies studied (Figure 24).

The calculated potential energy barriers for C–H insertion are higher than all subsequent calculated barriers along the reaction coordinate for both the Zr + C_2H_4 and Nb + C_2H_4 (Figures 1 and 2). Following C–H insertion, rearrangement and H_2 elimination is very favorable, whereas decay back to $M + C_2H_4$ requires passage back over a relatively tight transition state. Therefore, the sharply backward-scattered signal observed for Nb at all collision energies and for Zr at higher collision energies is attributed primarily to decay of MC_2H_4 complexes back to reactants, rather than from decay of HMC_2H_3 insertion intermediates.

At $E_{\text{coll}} = 6.0$ kcal/mol, although the reaction $M + C_2H_4 \rightarrow MC_2H_2 + H_2$ proceeds readily for both Nb and Zr with similar cross-sections, no significant wide-angle contribution from decay of ZrC_2H_4 complexes back to $Zr + C_2H_4$ is observed. Note that the hard sphere collision cross-sections with ethylene should be comparable for both atoms. Our finding that $Zr + C_2H_4 \rightarrow ZrC_2H_2 + H_2$ proceeds readily at low collision energies *without* reformation of Zr from ZrC_2H_4 complexes implies either (1) all ZrC_2H_4 complexes formed at low collision energies proceed to dehydrogenation products, or (2) ZrC_2H_4 complexes are *not* formed at low collision energies and all reactions proceed via direct C–H bond insertion. We now explore these two possibilities in some detail.

According to the recent electronic structure calculations, the barrier for Zr insertion forming $HZrC_2H_3$ lies 1.8 kcal/mol *above* the $Zr + C_2H_4$ asymptote, whereas the analogous barrier for Nb insertion lies 1.3 kcal/mol *lower* than Nb + C_2H_4 .¹³ On the basis of these C–H insertion barrier heights, it would be expected that ZrC_2H_4 complexes should be *less* likely to undergo C–H insertion than NbC_2H_4 at low collision energies. Indeed, Carroll and co-workers find that Zr is considerably less reactive than Nb at room temperature.¹³ Although the Nb reaction ultimately requires a spin flip, Carroll's observation that Nb + C_2H_4 reacts on nearly every gas kinetic collision indicates that the crossing to the quartet surface is facile at low collision energies. Therefore, the observation that decay back to reactants is seen for Nb but not for Zr at low collision energies is *not* likely to be attributable to a bottleneck for intersystem crossing in the Nb case.

RRKM calculations⁴³ were undertaken to determine the unimolecular reaction rate constant for dissociation of the ZrC_2H_4 metallacyclopropane complex back to reactants (k_{diss}) assuming no barrier to decay in excess of the $Zr + C_2H_4$

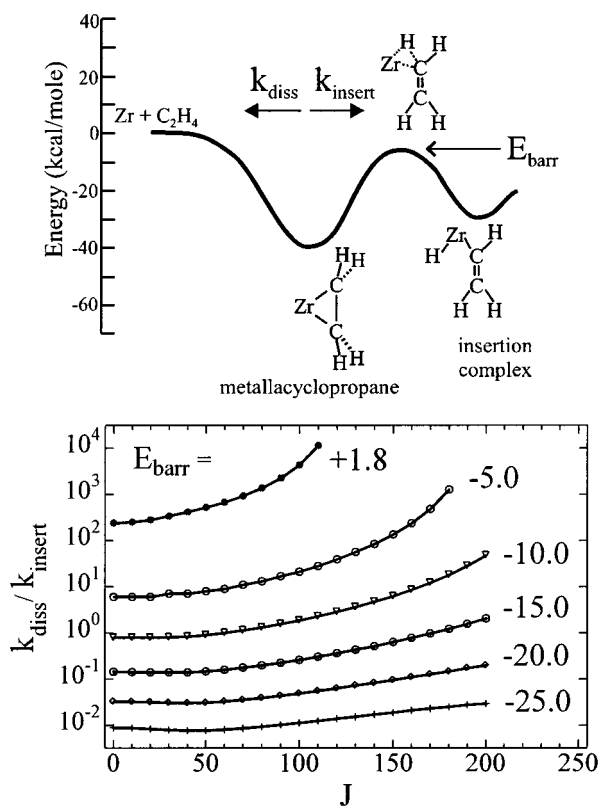


Figure 26. Simplified energy diagram for unimolecular decomposition of ZrC_2H_4 complexes at $E_{\text{coll}} = 6.0$ kcal/mol. Complexes may dissociate back to reactants (k_{diss}) or undergo C–H insertion (k_{insert}). Lower panel shows ratio of reaction rate constants for competing channels as function of E_{barr} , defined as the height of the C–H insertion barrier relative to separated $Zr + C_2H_4$ reactants.

asymptote. The rate constant for C–H bond insertion (k_{insert}) was also calculated as a function of the barrier height for insertion (E_{barr} ; see Figure 26). The ratio of the reaction rate constants ($k_{\text{diss}}/k_{\text{insert}}$) was then computed. The geometry and 15 vibrational frequencies used for modeling the ZrC_2H_4 metallacyclopropane complex were those calculated by Siegbahn and have been reported elsewhere.⁴¹ Decay back to reactants proceeds via a loose transition state, with the Zr atom located at a distance $R^\ddagger(J)$ from the ethylene molecule. $R^\ddagger(J)$ was calculated as the position of the maximum in the long-range effective potential (eq 4) for each orbital angular momentum J considered. Two of the rotations of the ethylene molecule, corresponding to "rocks", were treated as active rotations, and angular momentum was conserved during dissociation. The vibrations used for the loose transition state were the 12 highest frequency vibrations of the complex (which are very similar, but slightly perturbed in comparison to the 12 vibrations of the ethylene molecule), as suggested by Carroll.⁴¹ The geometry of the tight transition state leading to insertion products has also been calculated by Siegbahn, although the vibrational frequencies have not been reported.¹⁹ As an estimate of these, the vibrational modes of the metallacyclopropane complex were used, with one of the low-frequency vibrations (corresponding to the reaction coordinate) removed. Angular momentum conservation was also obeyed for the insertion process.

The results of the RRKM modeling at an energy of 6 kcal/mol above the separated $Zr + C_2H_4$ reactants are summarized in Figure 26. Using the *ab initio* insertion barrier height (E_{barr}) of +1.8 kcal/mol, the rate constant for dissociation is 2–4 orders of magnitude greater than that for insertion. Clearly, by lowering the barrier for insertion (i.e., more negative values of E_{barr}), the

ratio of dissociation to insertion ($k_{\text{diss}}/k_{\text{insert}}$) decreases. However, to reproduce the experimental observations (Figure 24), this ratio must become smaller than 0.05, requiring the barrier for insertion to be below -20 kcal/mol. It seems very unlikely that the calculated value of $+1.8$ kcal/mol¹³ could be so grossly in error. Furthermore, if the barrier for C–H insertion was so low, it would be difficult to rationalize the abrupt onset of strong wide-angle Zr nonreactive scattering from decay of complexes back to reactants at $E_{\text{coll}} \geq 9$ kcal/mol. Hence, it is not possible to explain the observed lack of backward scattered Zr atoms at low collision energies using a model involving barrierless association through a loose transition state for $\text{Zr} + \text{C}_2\text{H}_4$. Thus, we conclude that there exists a barrier leading to ZrC_2H_4 formation that is not present in the analogous case of NbC_2H_4 complex formation.

Clearly, the inert gaslike s^2 ground state electronic configuration of Zr may lead to a barrier for complex formation that is not likely to be present for Nb, having an s^1 configuration.¹¹ As noted by Carroll et al., the height of the barrier for complex formation (Figure 1) is related to the magnitude of the energy spacing between the metal atom ground-state s^2 configuration (correlating to an excited state of the complex) and the low-spin excited state of the metal atom (correlating to the ground-state complex).¹¹ Furthermore, as noted in the Introduction, the ground-state ZrC_2H_4 complex is actually best described as a metallacyclopropane.^{13,18} Although several stationary points along the $\text{Zr} + \text{C}_2\text{H}_4$ reaction pathway have been calculated,^{13,18,19} the barrier height for formation of ground-state ZrC_2H_4 from separated $\text{Zr} + \text{C}_2\text{H}_4$ has not been calculated explicitly to date. The observation that Zr is removed by C_2H_4 in one out of five gas kinetic collisions at room temperature has been taken as supporting evidence for a barrier to reaction no larger than 2 kcal/mol,^{11,13,14} but the location of the barrier along the reaction coordinate has not been determined experimentally.

We have performed additional RRKM calculations that assumed a barrier of 2 kcal/mol for $\text{Zr} + \text{C}_2\text{H}_4 \rightarrow \text{ZrC}_2\text{H}_4$. In this case, the transition state for association was modeled as tight. Since no transition state vibrational frequencies were available, they were estimated to be the same as those of the complex, with the lowest frequency vibration removed. Therefore, these calculations address only the effects of relative barrier heights and moments of inertia on $k_{\text{diss}}/k_{\text{insert}}$. In the absence of transition state vibrational frequencies, we cannot quantitatively assess the effects of the different vibrational frequencies at the respective transition states. In order to reproduce our finding that there is no decay of ZrC_2H_4 back to $\text{Zr} + \text{C}_2\text{H}_4$ at low collision energies, it is again necessary for the insertion barrier to be lower than the barrier for decay back to reactants. Using a C–H insertion barrier of -5 kcal/mol and a barrier of 2 kcal/mol for decay back to reactants, $k_{\text{diss}}/k_{\text{insert}} \approx 0.05$ at $E_{\text{coll}} = 6$ kcal/mol. Figure 27 displays the effective centrifugal barriers for various J values, assuming an insertion barrier of -5 kcal/mol. Note that higher collision energies open up reaction to larger J values capable of surmounting the centrifugal barrier for association. The larger moments of inertia of the association transition state (calculated in Figure 27 assuming Zr is located 4 \AA from C_2H_4) relative to those of the insertion transition state give rise to *smaller* centrifugal barriers for decay back to reactants. Thus at low collision energies, provided that the barrier for C–H insertion is below that for dissociation back to $\text{Zr} + \text{C}_2\text{H}_4$, insertion is the dominant channel, in agreement with our experimental observations. At the larger values of J accessible at higher collision energies, dissociation back to Zr

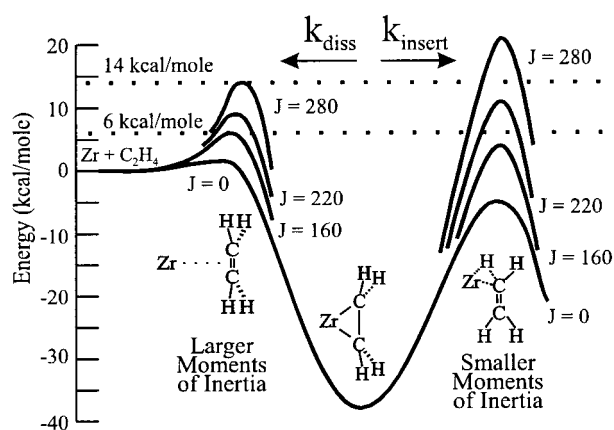


Figure 27. Effective potential for ZrC_2H_4 association and C–H insertion as a function of total angular momentum quantum number J , assuming a 2 kcal/mol association barrier and a C–H insertion transition state at -5 kcal/mol.

+ C_2H_4 becomes significant because of the smaller effective barrier for this process relative to that for C–H insertion. Similar behavior has been implicated in recent studies of $\text{Ni}^+ + \text{C}_3\text{H}_8$.⁴⁴ At large values of J , reaction rate constants for decay back to $\text{Ni}^+ + \text{C}_3\text{H}_8$ were calculated to greatly exceed those for C–H or C–C bond insertion.⁴⁴

Our RRKM modeling of the $\text{Zr} + \text{C}_2\text{H}_4$ system indicates that the C–H insertion barrier must be *lower* than the association barrier. This modeling of the competition between ZrC_2H_4 decay back to $\text{Zr} + \text{C}_2\text{H}_4$ reactants and insertion into the C–H bond has utilized tight transition states for each process. Since the transition state for dissociation back to $\text{Zr} + \text{C}_2\text{H}_4$ is expected to be considerably “looser” than that for C–H insertion, it is likely that our model overestimates the fraction of complexes undergoing C–H insertion. Thus, the energetic difference between the ZrC_2H_4 association barrier and the C–H insertion barrier is likely to be even greater than the 7 kcal/mole difference required to simulate our experimental data using this model.

Given that the C–H insertion barrier clearly lies below that for association, we expect that certain $\text{Zr} + \text{C}_2\text{H}_4$ collision geometries may lead to *direct* C–H bond insertion without first accessing the ZrC_2H_4 well. It is important to note that our RRKM modeling of the $\text{Zr} + \text{C}_2\text{H}_4$ system has assumed that all reactivity occurs through initial formation of ZrC_2H_4 complexes prior to C–H insertion. In carrying out the tight association transition state calculations, we have assumed a barrier height of 2 kcal/mol, the largest barrier to H_2 elimination determined in experiments carried out at room temperature by Weisshaar and co-workers.^{11,13,14} The additional possibility exists that the barrier to ZrC_2H_4 complex formation lies even higher than 2 kcal/mol, and most, if not all formation of H_2 elimination products at low collision energies, including the room temperature studies, results from direct C–H insertion without initial formation of ZrC_2H_4 complexes. Unlike in the Nb + ethylene system, this process is not inhibited by the need for a spin flip, as both the reaction coordinate and ground state Zr reactant are of triplet spin multiplicity. Indeed, Siegbahn and co-workers have pointed out that the calculated geometry of the metallacyclopropane complex differs considerably from the transition state geometry for C–H insertion.¹⁹ In particular, the metallacyclopropane complex (of C_{2v} symmetry) corresponds to a metal atom lying above the plane of a C_2H_4 molecule with a considerably lengthened C–C bond and hydrogen atoms distorted away from the metal atom (Figure 27).¹⁸ The transition state for C–H insertion, on the other hand, has a relatively short C=C bond distance similar to that in free C_2H_4 , with the metal

atom lying near the plane of C_2H_4 , indicating that no strong chemical interaction exists between Zr and the C–C π -bond at the transition state for C–H insertion.¹⁹ Consequently, the height of the barrier for direct C–H insertion, without initial formation of a metallacyclopropane, is also likely to lie below the asymptotic energy of the $Zr + C_2H_4$ reactants. In this regard it is interesting to note that Stoutland and Bergman⁴⁵ have studied the reaction $(\eta^5-C_5Me_5)(PMe_3)Ir + C_2H_4$ in solution. Their results indicated the involvement of a direct insertion reaction without the initial formation of a complex, as well as a separate channel forming complexes. Subsequent extended Hückel calculations suggest that the most favorable approach of the metal center for insertion is along the H–C bond axis in ethylene.⁴⁶ Further calculations on the $Zr + C_2H_4$ system focusing on transition states for direct C–H bond insertion and insertion starting from ZrC_2H_4 would be interesting.

In the case of the Nb reaction, at the lowest studied collision energy of 4.8 kcal/mol, decay of complexes is clearly observed. In addition to reforming reactants, these complexes can readily undergo intersystem crossing and then C–H insertion. Direct C–H bond insertion by Nb is likely to be inhibited by spin conservation. The intersystem crossing necessary for C–H bond insertion by Nb is enhanced by multiple recrossings in the region of the surface crossing for long-lived NbC_2H_4 complexes. Such complex-mediated spin-forbidden processes in bimolecular reactions are well-known, for example, $Ba + SO_2$.⁴⁷

Comparison of Nb and Zr Reactivity. At 6 kcal/mol, the reactivities of Nb and Zr are comparable (Figure 25). However, there is a clear trend toward greater reactivity of Nb with decreasing collision energies. This trend is in agreement with the room-temperature flow-tube result of Carroll et al.¹³ Under the conditions of their experiment, corresponding to a mean collision energy of approximately 0.9 kcal/mol, ground state Nb was depleted by ethylene approximately five times more efficiently than ground-state Zr (i.e., $k_{diss}/k_{insert} = 0.2$). The greater reactivity of Nb at low collision energies is attributable to the absence of any significant barrier above the ground-state reactants for complex formation, leading to a large capture cross-section. Because the C–H insertion barrier for Nb lies below the reactants, a substantial fraction of these complexes go on to insertion and H_2 elimination.

At increasing collision energies, we find that Zr becomes increasingly more reactive than Nb (Figure 25). In the case of $Zr + C_2H_4$, the presence of an association barrier will lead to a large increase in the efficiency of complex formation with increasing collision energy. Once complexes are formed, C–H insertion is the dominant fate because of the relatively tight transition state for decay back to reactants and the low barrier for C–H insertion. In the case of $Nb + C_2H_4$, because no association barrier is present, complex formation is efficient even at low collision energies. However, since the transition state for decay back to reactants is expected to be looser than for Zr, a larger fraction of NbC_2H_4 complexes decay back to reactants. Note again that direct C–H insertion without initial formation of ZrC_2H_4 complexes may play an important role for $Zr + C_2H_4$, particularly for small impact parameter collisions where the barrier for C–H insertion is likely to be considerably smaller than for association (Figure 27).

V. Conclusions

The reactions of ground-state transition metal (M) atoms Zr and Nb with ethylene (C_2H_4) were studied using the technique of crossed molecular beams. Reactions forming $MC_2H_2 + H_2$ involve intermediate complexes with lifetimes longer than their

rotational periods. Wide-angle inelastic scattering of atomic M resulting from the decay of long-lived MC_2H_4 complexes was also observed for both transition metal reactants. For the Zr system, this was only observed for $E_{coll} \geq 9.1$ kcal/mol, indicating that an adiabatic barrier exists for formation of ZrC_2H_4 complexes. RRKM calculations modeling the competition between decay back to $Zr + C_2H_4$ reactants and C–H bond insertion require that the insertion barrier be lower than the barrier for association. Reaction of Zr atoms at low collision energies via initial formation of ZrC_2H_4 is likely to be hindered by this barrier to association. The Nb reaction can occur at low collision energies by initial NbC_2H_4 complex formation without a barrier above reactants, which facilitates the spin flip necessary for C–H bond insertion. At increasing energies, Zr becomes the more reactive atom as the barrier for complex formation is surmounted. Alternatively, direct C–H insertion without metallacyclopropane formation is fully spin-allowed in the $Zr + C_2H_4$ reaction and may play an important role. Our finding that the barrier for C–H insertion must be below that for ZrC_2H_4 formation suggests that such a direct mechanism is in fact likely.

Future experiments include a more quantitative determination of the branching ratios between nonreaction and reaction as a function of collision energy. These studies, together with careful modeling, should facilitate a precise determination of the potential energy barrier for ZrC_2H_4 complex formation and may better assess the role of direct C–H insertion.

Acknowledgment. This work was supported by a National Science Foundation Faculty Early Career Development Award, and by an NSF Equipment Grant. Some of the equipment used in this work was funded by an ONR Young Investigator Award. Support by the Exxon Educational Foundation is also gratefully acknowledged. H.S. thanks the Link Foundation for a Graduate Fellowship. R.H. thanks the Department of Education for a Graduate Fellowship. The authors thank B. Carpenter, J. Weisshaar, S. Klippenstein, and P. Wolczanski for valuable discussions and suggestions.

References and Notes

- (1) Anderson, J. R.; Boudart, M. *Catalysis: Science and Technology*; Springer-Verlag: Berlin, 1984; Vol. 6, Chapter 1.
- (2) Mathey, F.; Sevin, A. *Molecular Chemistry of the Transition Metal Elements*; John Wiley & Sons: New York, 1996; pp 189–192.
- (3) Crabtree, R. H. *The Organometallic Chemistry of the Transition Metals*; John Wiley & Sons: New York, 1988; pp 267–275.
- (4) (a) Siegbahn, P. E. M.; Blomberg, M. R. A. In *Theoretical Aspects of Homogeneous Catalysis*; van Leeuwen, P. W. N. M., Morokuma, K., van Lenthe, J. H., Eds.; Kluwer Academic Publishers: Dordrecht, 1995; p 15–63. (b) Wittborn, A. M. C.; Costas, M.; Blomberg, M. R. A.; Siegbahn, P. E. M. *J. Chem. Phys.* **1997**, *107*, 4318. (c) Blomberg, M. R. A.; Siegbahn, P. E. M.; Svensson, M. *J. Am. Chem. Soc.* **1992**, *114*, 6095. (d) Siegbahn, P. E. M. *J. Phys. Chem.* **1995**, *99*, 12723. (e) Blomberg, M. R. A.; Siegbahn, P. E. M.; Svensson, M. *J. Am. Chem. Soc.* **1992**, *114* (4), 6095. (f) Blomberg, M. R. A.; Siegbahn, P. E. M.; Nagashima, U.; Wennerberg, J. *J. Am. Chem. Soc.* **1991**, *113*, 424. (g) Siegbahn, P. E. M. *Chem. Phys. Lett.* **1993**, *205*, 290.
- (5) (a) Siegbahn, P. E. M.; Blomberg, M. R. A.; Svensson, M. *J. Am. Chem. Soc.* **1993**, *115*, 4191. (b) Siegbahn, P. E. M. *J. Am. Chem. Soc.* **1993**, *115*, 5803. (c) Siegbahn, P. E. M. *J. Organomet. Chem.* **1995**, *491*, 231.
- (6) Low, J. J.; Goddard, W. A. (a) *Organometallics* **1986**, *5*, 609. (b) *J. Am. Chem. Soc.* **1984**, *106*, 8321. (c) *J. Am. Chem. Soc.* **1984**, *106*, 6928. (d) *J. Am. Chem. Soc.* **1986**, *108*, 6115.
- (7) (a) Bauschlicher, C. W., Jr.; Langhoff, S. R.; Partridge, H.; Barnes, L. A. *J. Chem. Phys.* **1989**, *91*, 2399. (b) Rosi, M.; Bauschlicher, C. W., Jr.; Langhoff, S. R.; Partridge, J. J. *Phys. Chem.* **1990**, *94*, 8656.
- (8) (a) Weisshaar, J. C. *Adv. Chem. Phys.* **1992**, *82*, 213. (b) Weisshaar, J. C. *Acc. Chem. Res.* **1993**, *26*, 213.
- (9) Armentrout, P. B.; Kickel, B. L. *Organometallic Ion Chemistry*; Freiser, B. S., Ed.; Kluwer Academic Publishers: Dordrecht, 1996; pp 1–45.

- (10) Armentrout, P. B. (a) *Annu. Rev. Phys. Chem.* **1990**, *41*, 313. (b) *Polyhedron* **1988**, *7*, 1573. (c) *Science*, **1991**, *251*, 175. (d) Georgiadis, R.; Armentrout, P. B. *J. Phys. Chem.* **1988**, *92*, 7060.
- (11) (a) Carroll, J. J.; Haug, K. L.; Weisshaar, J. C. *J. Am. Chem. Soc.* **1993**, *115*, 6962. (b) Carroll, J. J.; Weisshaar, J. C. *J. Phys. Chem.* **1996**, *100*, 12355. (c) Ritter, D.; Carroll, J. J.; Weisshaar, J. C. *J. Phys. Chem.* **1992**, *96*, 10636.
- (12) Carroll, J. J.; Weisshaar, J. C.; Siegbahn, P. E. M.; Wittborn, C. A. M.; Blomberg, M. R. A. *J. Phys. Chem.* **1995**, *99*, 14388.
- (13) Carroll, J. J.; Hauge, K. L.; Weisshaar, J. C.; Blomberg, M. R. A.; Siegbahn, P. E. M.; Svensson, M. *J. Phys. Chem.* **1995**, *99*, 13955.
- (14) Wen, Y.; Porembski, M.; Ferrett, T. A.; Weisshaar, J. C. *J. Phys. Chem. A* **1998**, *102*, 8362.
- (15) (a) Lian, L.; Mitchell, S. A.; Rayner, D. M. *J. Phys. Chem.* **1994**, *98*, 11637. (b) Brown, C. E.; Mitchell, S. A.; Hackett, P. A. *Chem. Phys. Lett.* **1992**, *191*, 175.
- (16) (a) Mitchell, S. A.; Hackett, P. A. *J. Chem. Phys.* **1990**, *93*, 7822. (b) Blitz, M. A.; Mitchell, S. A.; Hackett, P. A. *J. Phys. Chem.* **1991**, *95*, 8719. (c) Mitchell, S. A. *Gas-Phase Metal Reactions*; Fontijn, A., Ed.; North-Holland: Amsterdam, 1992; Chapter 12.
- (17) Campbell, M. L. (a) *J. Chem. Soc., Faraday Trans.* **1998**, *94*, 353. (b) *J. Phys. Chem. A* **1998**, *102*, 892. (c) *J. Phys. Chem. A* **1997**, *101*, 9377. (d) *J. Am. Chem. Soc.* **1997**, *119*, 5984.
- (18) Blomberg, M. R. A.; Siegbahn, P. E. M.; Svensson, M. *J. Phys. Chem.* **1992**, *96*, 9794.
- (19) Siegbahn, P. E. M.; Blomberg, M. R. A.; Svensson, M. *J. Am. Chem. Soc.* **1993**, *115*, 1952.
- (20) Papai, I.; Mink, J.; Fournier R.; Salahub, D. R. *J. Phys. Chem.* **1993**, *97*, 9986.
- (21) (a) Widmark, P.; Roos, B. O.; Siegbahn, P. E. M. *J. Phys. Chem.* **1985**, *89*, 2180. (b) Pierloot, K.; Persson B. J.; Roos, B. O. *J. Phys. Chem.* **1995**, *99*, 3465.
- (22) Blomberg, M. R. A.; Siegbahn, P. E. M.; Lee, T. J.; Rendell, A. P.; Rice, J. E. *J. Chem. Phys.* **1991**, *95*, 5898. (b) Blomberg, M. R. A.; Siegbahn, P. E. M.; *J. Chem. Phys.* **1983**, *78*, 5682.
- (23) Willis, P. A.; Stauffer, H. U.; Hinrichs, R. Z.; Davis, H. F. *J. Chem. Phys.* **1998**, *108*, 2665.
- (24) Willis, P. A.; Stauffer, H. U.; Hinrichs, R. Z.; Davis, H. F. *Laser Techniques for State-Selected and State-to-State Chemistry IV*; SPIE Conference Proceedings, 1998; p 3271.
- (25) Willis, P. A.; Stauffer, H. U.; Hinrichs, R. Z.; Davis, H. F. *Rev. Sci. Instrum.*, accepted for publication.
- (26) (a) Chatt, J.; Duncanson, L. A. *J. Chem. Soc.* **1953**, 2939. (b) Dewar, M. J. S. *Bull. Soc. Chim. Fr.* **1951**, 79.
- (27) Bader, R. F. W.; Gangi, R. A. *J. Am. Chem. Soc.* **1971**, *93*, 1831.
- (28) Gupta, S. K.; Gingerich, K. A. *J. Chem. Phys.* **1981**, *74*, 3584.
- (29) Chase, M. W., Jr.; Davies, C. A.; Downey, J. R.; Frurip, D. J.; McDonald, R. A.; Syverud, A. N. *J. Phys. Chem. Ref. Data*, **1981**, *13*, Suppl. 1. — *JANAF Thermochemical Tables*, 3rd ed.
- (30) Powers, D. E.; Hansen, S. G.; Geusic, M. E.; Puiu, A. C.; Hopkins, J. B.; Dietz, T. G.; Duncan, M. A.; Langridge-Smith P. R. R.; Smalley R. E. *J. Phys. Chem.* **1982**, *86*, 2556.
- (31) Proch D.; Trickl, T. *Rev. Sci. Instrum.* **1989**, *60*, 713.
- (32) Lee, Y. T.; McDonald, J. D.; LeBreton, P. R.; Herschbach, D. R. *Rev. Sci. Instrum.* **1969**, *40*, 1402.
- (33) Stauffer, H. U., unpublished.
- (34) Miller, W. B.; Safron, S. A.; Herschbach, D. R. (a) *Discuss. Faraday Soc.* **1967**, *44*, 108. (b) *J. Chem. Phys.* **1972**, *56*, 3581.
- (35) Moore, C. E. *Atomic Energy Levels*; National Bureau of Standards: Washington DC, 1971.
- (36) Corliss C. H.; Bozman, W. R. *Experimental Transition Probabilities*; National Bureau of Standards: Washington DC, 1962.
- (37) *C. R. C. Handbook of Chemistry and Physics*, 75th ed.; Lide, D. R., Ed.; CRC Press: Boca Raton, FL, 1994–1995.
- (38) Levine, R. D.; Bernstein, R. B. *Molecular Reaction Dynamics and Chemical Reactivity*, Oxford University Press: Oxford, 1987; pp 412–417.
- (39) Scoles, G. *Atomic and Molecular Beam Methods*; Oxford University Press: New York, 1988; Vol. 1, Chapter 1.
- (40) Johnston, H. S. *Chemical Reaction Rate Theory*; Ronald Press: New York, 1966.
- (41) Carroll, J. J., Ph.D. Thesis, University of Wisconsin—Madison, 1995.
- (42) Cambi, R.; Cappelletti, D.; Liuti, G.; and Pirani, F. *J. Chem. Phys.* **1991**, *95*, 1852.
- (43) Zhu, L.; Hase, W. L. Program #644, Quantum Chemistry Program Exchange, Indiana University.
- (44) Yi, S. S.; Blomberg, M. R. A.; Siegbahn, P. E. M.; Weisshaar, J. C. *J. Phys. Chem. A* **1998**, *102*, 395.
- (45) (a) Stoutland P. O.; Bergman, R. G. *J. Am. Chem. Soc.* **1985**, *107*, 4581. (b) Stoutland P. O.; Bergman, R. G. *J. Am. Chem. Soc.* **1988**, *110*, 5732.
- (46) Silvestre, J.; Calhorda, M. J.; Hoffmann, R.; Stoutland, P. O.; Bergman, R. G. *Organometallics*, **1986**, *5*, 1841.
- (47) (a) Smith, G. P.; Zare, R. N. *J. Am. Chem. Soc.* **1975**, *97*, 1985. (b) Freedman, A.; Parr, T. P.; Behrens, R.; Herm, R. R. *J. Chem. Phys.* **1979**, *70*, 5251.